University of Stavanger

FACULTY OF SCIENCE AND TECHNOLOGY

MASTER'S THESIS

Study programme: Petroleum Geosciences Engineering	Spring semester, 2018 Open
Author: Maria Antonieta Alcantara Rodriguez	..... (signature of author)
Supervisor(s): Wiktor Waldemar Weibull	
Title of master's thesis: Ground penetrating radar and seismic study to determine glacial deposit stratigraphy	
Credits: 30	
Keywords: Ground Penetrating Radar Seismic acquisition Near-surface geophysics Glacial deposits Jæren	Number of pages: 86 Stavanger, 15 June 2018 date/year

Ground penetrating radar and seismic study to determine glacial deposit stratigraphy

by

Maria Antonieta Alcantara Rodriguez

Master Thesis

Presented to the Faculty of Science and Technology

The University of Stavanger

University of Stavanger

June, 2018

Dedication

I dedicate this work to the special people in my life, this goes to my family in Mexico especially my parents Alberto and Maria Antonieta, my siblings Alberto and Maiella, to my nephews and niece, Santiago, Manuel and Maria Fernanda, and to Beatriz and Manuel. Thank you all for your unconditional love and support from the other side of the world.

To my husband, Austin Bingham for providing me with unfailing support and continuous encouragement throughout this roller coaster, what can I say except: Thank you!

To the people who became my family away from home: Natalia and Erick, thank you for always being there for me. And to my Mexicans in Norway: Diana, Pablo, Roberto, Alex and Obed (even though most of you are not here anymore).

To the one and only Diana Rosado for being my cheerleader and therapist in the difficult times.

And a special note for the geonerds and tea buddies, thank you for helping me readjust to the student life.

This accomplishment would not have been possible without any of you.

Thank you.

Maria Antonieta Alcantara Rodriguez

Acknowledgments

I would first like to thank my thesis advisor Wiktor Waldemar Weibull of the Faculty of Science and Technology at The University of Stavanger. His valuable advice helped me push this work in the right direction.

I would also like to thank the people who took part in the acquisition brigades: Karen Synnøve Ohm, Nestor Cardozo, Paul Nadeau, Fernando Mazuera and Diego Lopez Mulero, and once again Wiktor Waldemar Weibull for taking care of the logistics for the acquisition.

To Dmitry Shogin From the University of Stavanger for his valuable help with LaTeX.

I would also like to acknowledge the experts who took part in the validation of the first geological interpretation for the Undheim area: Bjørn Kåre Bryn from Spirit Energy/ FORCE and Alejandro Escalona from the University of Stavanger. With their participation and input, the geological model is closer to reality. And to Matthew Lane from Spirit Energy for his input in the geological model workflow.

Abstract

Ground penetrating radar and seismic study to determine glacial deposit stratigraphy

María Antonieta Alcántara Rodríguez, MSc
The University of Stavanger, 2018
Supervisor: Wiktor Waldemar Weibull

This work reviews two near-surface geophysical methods, ground penetrating radar and seismic, covering all the processes from the data acquisition to the interpretation. The area of study, Jæren, is located over glacial deposits, which will be mapped in this work across three locations. The depth of the basement was also interpreted as a result from this study.

The problems related to the acquisition are discussed, and the advantages/ disadvantages of each method are debated. A processing workflow is derived from this study as a guideline for future work with radar data.

Ground penetrating radar and seismic inversion are combined with the aim of obtaining a robust model to validate the results.

It is hoped that this study will serve as a guideline for future geophysical studies using the equipment available at the University of Stavanger.

Table of Contents

List of Figures

List of Tables

1. Introduction

Near surface geophysical methods are widely used in several industries, such as engineering, archaeology, and construction. The two geophysical methods used in this work are ground penetrating radar (GPR) and refraction seismic. Given the geological characteristics of the explored area and the source used, these methods provide results up to 40 m deep. Surface processes shaped the Norwegian landscape during the Quaternary through glaciations, and the southwestern coast contains large glacier deposits. The Jæren area is mainly composed of moraine and glaciofluvial deposits.

This work has two main objectives. The first objective is to create a depth to the basement map of three different areas with distinct lithologies using two geophysical exploration methods. The second objective is to perform a subsurface interpretation of the glacial deposits in the area.

All the steps of these methods are covered in this work, from acquisition, processing, interpretation, and finally a combination of the generated models to achieve a final result.

GPR acquisition could be performed in a short amount of time. The equipment had to be assembled and the acquisition only took the time needed to walk the desired line. There were no weather requirements and no special extra equipment is needed. On the other hand, seismic acquisition required a longer preparation since it has several restrictions. For example, it has to avoid ambient noise as much as possible, which can be a difficult situation since the average precipitation per month in the area is between 100 and 200 mm (information from The Norwegian Water Resources and Energy Directorate, 2018). Similarly, the geophones have to be grounded and with freezing temperatures, the soil was not easy to drill to perform this task. The acquisition of a 200 m seismic line required a full day, and extra equipment was necessary such as a generator to power the recording system, a sledgehammer to act as source, and special drilling equipment to place the geophones.

The existing literature in the combination of both methods use the common mid point radar acquisition (Booth et al., 2013) which was not part of the extent of this work so the comparison of results is not feasible.

2. Geological setting

The area of study is located near the coast of SW Norway, in the Jæren region, Figure 1. Based on the sediment sequence and seabed morphology in the Norwegian Channel, deposits on the North Sea Fan, and morphology and deposits on Jæren, it is now generally accepted that a fast-flowing ice stream was active in the Norwegian Channel (Norwegian Channel Ice Stream, NCIS) several times during the Quaternary and inundated the western part of Jæren. The existing glacial deposits in the coastal area indicate glacial advance at least once, followed by an ice-retreat/interstadial phase and another ice advance that crossed the coastline depositing a till. Marine deposits that are in high areas in Jæren indicate deposition during a state of glacioisostatic depression. During a substantial portion of the Quaternary, glaciers and ice caps were restricted to mountain areas. During glaciations, ice divides, ice-marginal, erosional, and depositional zones have been migrating and affected the landscape at various locations (Fredin et al., 2013, Knudsen, Larsen, Sejrup, and Stalsberg, 2006 and Olsen, Sveian, Ottesen, and Rise, 2013).

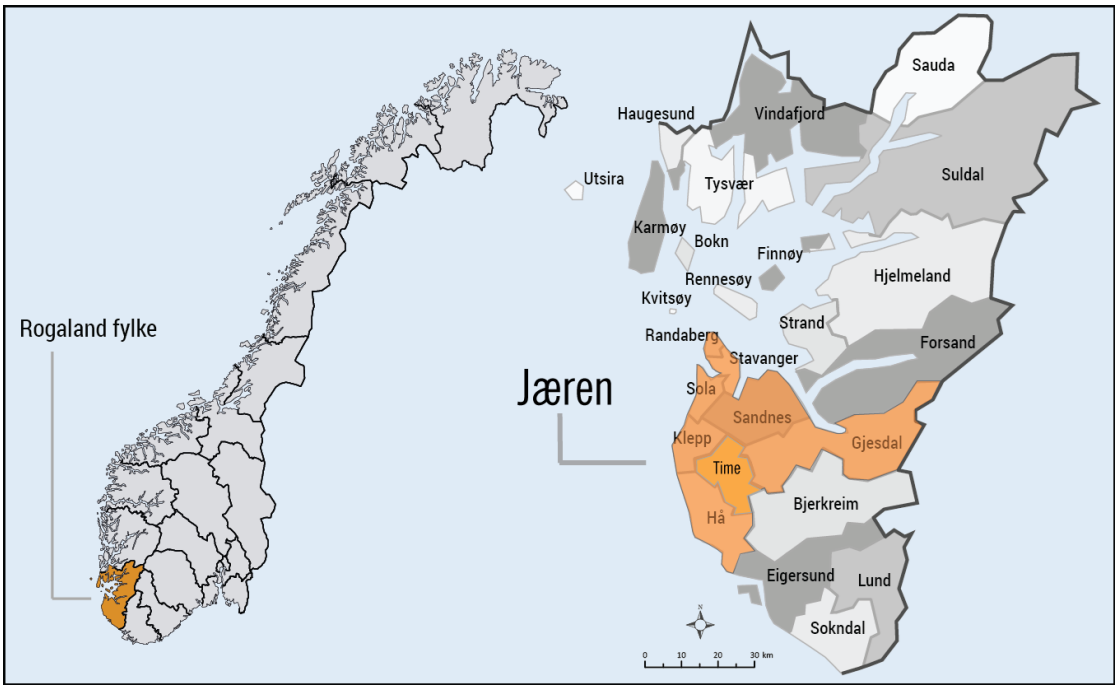

Figure 1: Jæren location in SW Norway (Modified from Helleve, 2017).

The Jæren area has been described as the border zone between the marine-based ice

stream in the Norwegian Channel and the terrestrial sheet inland. The surface sediments in the southwestern part of Jæren are dominated by clay-rich till, with intercalation of marine and glaciomarine sediments, while sandy and gravelly tills prevail in the northern and eastern part. Based on outcrops, excavations, drillings, and some seismic profiles, the average sediment thickness in areas with a continuous cover of sediments is estimated to be around 6 m. Both types of till are underlain by glaciomarine sediments deposited during the Sandnes interstadial about 30,000-35,000 years ago (Raunholm, Sejrup, and Larsen, 2003 and Olsen et al., 2013).

As discussed in Birkeland, 1981, most of rocks in the Jæren area belong to a Caledonian nappe system that has been thrust directly upon the Precambrian basement. The allochthon consists of four discrete nappe sheets of different lithology, tectonic style, and metamorphic grade (Figure 2).

The lowermost thrust unit, the Lower Nappe Sheet, is mainly composed of phyllites, with smaller amounts of metaclastics. This nappe presents a complicated fold pattern, with a major direction of folding along the NW-SE trending axes.

The next tectonic unit is heterogeneous, with gneisses and feldspathic schists as the dominant rock members. The contact of this nappe with the previous is usually marked as slice-shaped bodies of gneiss and feldspathic schist alternating with thicker and thinner masses of garnet-bearing phyllite. This unit is known as the Boknfjorden Nappe Complex.

A third one, the Jæren Nappe Complex, composed of medium amphibolite facies supracrustals and granitoid plutonites of anatectic derivation, overlies both two mentioned nappes. This complex may be characterized as a N-S oriented sinuous fold system. In the northern part of Figure 2, most of the rock masses of this nappe have been worn away. Structurally, the Jæren Nappe Complex is characterized as a N-S oriented sinuous fold system.

The Karmsund Nappe is the highest tectonic unit within the nappe system. It is located at the west and northwest of Jæren, is mainly composed of greenschist facies metabasites of Early Ordovician age and is in a N-S trending zone.

The Precambrian basement is located at the East of the Jæren district. It can be identified by a great expanse of mountain country dominated by massive, often granite-looking

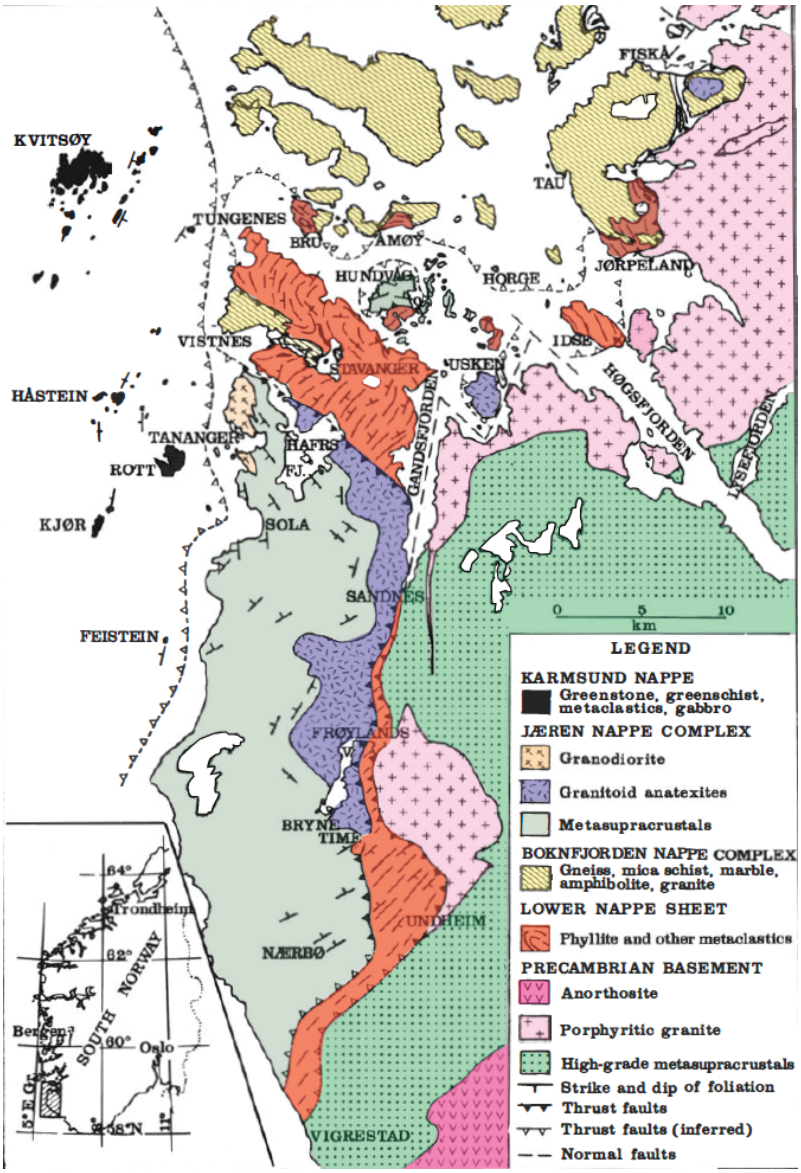

Figure 2: Geological-tectonic map of Jæren. Modified from Birkeland, 1981.

gneisses, which have been invaded by large bodies of a coarse-grained granite of distinctly porphyritic character.

Jæren is in the confluence area of two different glacial regimes. When the ice stream filled the Norwegian Channel, land-based ice fed into it from the Northeast. Because of the deglaciation regimes, by analyzing the landforms it is possible to find the presence of Rogen moraines on the central area. These are assumed to have formed during the dynamical readvance caused by a rapid breakup of the Norwegian Channel. The marginal ridges were formed even later by readvance of a local ice lobe. The southern part of Jæren is dominated by hummocky moraines, also formed during the last deglaciation (Knudsen

et al., 2006).

2.1. Quaternary glacial deposits

The classification of sediments deposited in glacial environments is done in two main groups: primary deposits, which are laid down by uniquely glacial agencies, and secondary deposits, which have undergone some form of reworking by non-glacial processes.

Primary deposits include tills deposited at the ice-bed interface or the sub-glacial traction zone by the combined processes of deformation, ploughing, lodgment, and melt-out.

Secondary deposits are composed of glacial debris that has been remobilized and deposited by gravitational flowage, stream flow, or other agencies (Benn and Evans, 2010).

The principal structures found on the areas of study examined in this thesis, are moraine, and glaciofluvial deposits as shown in Figure 3.

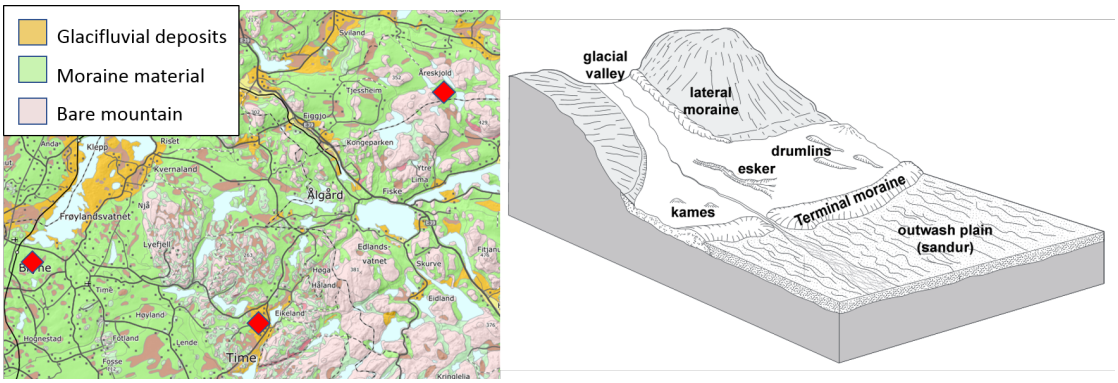

Figure 3: Left: Geological map of area of study, with locations marked in red. Right: Glacial landforms and deposits in continental glaciated areas (Nichols, 2009 p.107)

Moraines are accumulations of till formed directly at the margins of a glacier (Nichols, 2009). According to Benn and Evans, 2010, moraines can be divided in diverse types:

* End moraine, also called ice-marginal moraines, which mark the limit of glacial advance. They can be recognized as ridges, and they are formed at the glacier margin by glacier dumping of debris, ablation of debris or glaciotectonic processes.
* Push moraines formed where the glacier scrapes sediment from the valley floor, piling it up at the glacier front.

* Dump moraines formed at the snout of the glacier where the melting of ice keeps pace with glacial advance.

* Lateral moraines are created when a glacier retreats and the melting releases the detritus that has accumulated at the sides of the glacier where it is deposited.

* Hummocky moraine which is characterized by irregular morphology and sediment structure, typically formed at or on glaciers with a high content of debris.

Two of the three areas of study are located inside or next to a sand quarry. In the quarry located in Undheim, the sand is being extracted from a structural high, which leaves the structures of a moraine exposed. In Figure 4 it is possible to observe the end moraine structure with the main layers highlighted.

Figure 4: Moraine in Undheim with main structures marked.

Glaciofluvial deposits are sediments deposited from flowing water because of the seasonal abundance of meltwater. They manifest on channel floors as bedforms, of which there are four main types: plane beds, ripples, dunes, and antidunes (Benn and Evans, 2010).

Glacial depositional landforms are very susceptible to fluvial erosion shortly after the deglaciation due to little vegetation and unstable sediment structures (Fredin et al., 2013).

As discussed in Nichols, 2009, the glacial erosion processes result in a wide range of sizes of detrital particles. As the ice movement is a laminar flow there is no opportunity for various parts of the ice body to mix and hence no sorting of material carried by the glacier will take place. The main characteristics of glaciofluvial deposits are:

* Lithologies: mainly conglomerate, sandstone and mudstone.
* Mineralogy: variable, compositionally immature.
* texture: extremely poorly sorted in till to poorly sorted.
* Bed geometry: bedding absent to indistinct, may be laminated.
* Sedimentary structures: cross-bedding.
* Palaeocurrents: orientation of clasts can indicate ice flow direction.
* Fossils: may be present.
* Color: variable, but deposits may be oxidized.
* Facies associations: may be associated with fluvial facies or with shallow-marine deposits.

3. Ground Penetrating Radar

Ground penetrating radar is a noninvasive method using electromagnetic fields to probe lossy dielectric materials to detect structures and changes in material properties within the materials. GPR investigates the subsurface by making use of EM fields that propagate into the surface. EM fields that are time varying consist of coupled electric (E) and magnetic (H) fields.

GPR profiles, also called radargrams, are similar in appearance to seismic-reflection profiles, except that GPR data is acquired using transient electromagnetic energy reflection instead of acoustic energy and thus provide greater resolution. A short pulse of high-frequency EM energy is transmitted into the ground. When a signal encounters a contrast in material properties, some of the energy is reflected to the surface due to a change in the bulk electrical properties of different subsurface lithologies. Bedrock contact, organic-rich sediments, groundwater level, and changes in sediment grain size, mineralogy, and packing may characterize the interface between these layers. A change in the dielectric constant (relative permittivity) of the sediment also affects the rate of attenuation of energy passing through the ground (Jol, 2009).

The foundations of GPR lie in EM theory. Maxwell's equations mathematically describe the physics of EM fields. Constitutive relationships quantify material properties. Combining the two provides the foundations for quantitatively describing GPR signals (A. Annan, 2005 and Jol, 2009).

Maxwell's equations express EM fields and related properties as follow:

$$\nabla \times \mathbf{e} = -\frac{\partial \mathbf{b}}{\partial t} \tag{3.1}$$

$$\nabla \times \mathbf{h} = \mathbf{j} + \frac{\partial \mathbf{d}}{\partial t} \tag{3.2}$$

$$\nabla \cdot \mathbf{d} = \rho \tag{3.3}$$

$$\nabla \cdot \mathbf{b} = 0 \tag{3.4}$$

Where:

$\mathbf{e}$ = electric field strength vector (V/m)

$\mathbf{b}$ = magnetic flux density vector (T)

$\mathbf{d}$ = electric displacement vector (C/m^2)

$\mathbf{h}$ = magnetic field intensity (A/m)

ρ = electric charge density (C/m^2)

$\mathbf{j}$ = electric current density vector (A/m^2)

t = time (s)

The constitutive relationships are the means of relating the material physical properties to the EM fields. For GPR three quantities must be used:

* Electrical conductivity $\widetilde{\sigma}$

$$\mathbf{j} = \widetilde{\sigma}\mathbf{e} \tag{3.5}$$

describes how free charges flow to form a current when an electric field is present.

* Dielectric permitivity $\widetilde{\varepsilon}$

$$\mathbf{d} = \widetilde{\varepsilon}\mathbf{e} \tag{3.6}$$

describes how constrained charges are displaced in response to an electric field.

* Magnetic permeability $\widetilde{\mu}$

$$\mathbf{b} = \widetilde{\mu}\mathbf{h} \tag{3.7}$$

describes how intrinsic atomic and molecular magnetic moments respond to a magnetic field.

In general, $\widetilde{\sigma}$, $\widetilde{\varepsilon}$, and $\widetilde{\mu}$ are tensors and can be non-linear. For GPR issues, these quantities are treated as field independent scalar qualities. In other words, the response is in the same direction as the exciting field and independent of field strength (A. Annan, 2005).

The way electromagnetic fields interact with natural materials controls how electromagnetic fields spread into the medium and are attenuated in the medium. In addition, the variation in physical properties gives rise to the observed subsurface reflections obtained with a GPR system (P. Annan, 2003 and A. Annan, 2005).

Electrical displacement properties dominate conductive properties for most geological materials. Thus, radar velocity (v) can be approximated as:

$$v = \frac{c}{\sqrt{K}} = s^{-1} \tag{3.8}$$

where K is the rock's dielectric constant, c is the speed of light in air (0.3 m/ns), and slowness (s) is the reciprocal of velocity (Fisher, Stewart, and Jol, 1996).

Earth materials are invariably composites of many other materials or components. Water and ice represent the few cases where a single component is primarily present. Understanding the physical properties of mixtures is a key factor in the interpretation of a GPR response (Jol, 2009).

The greatest influences on radar-wave velocity are rock matrix porosity (ϕ) and pore fluid velocities. The matrix velocity can be assumed constant for most geological materials. Table 1 summarizes the relative permittivity and conductivity for some common materials encountered with GPR where **K** is the dielectric constant, σ is the electrical conductivity in mS/m, **v** is the velocity in m/ns, and **a** is the attenuation in dB/m. The presence or absence of water in the material dominates behavior (P. Annan, 2003 and Fisher et al., 1996).

Material	K	σ (mS/m)	v (m/ns)	a (dB/m)
Air	1	0	0.30	0
Distilled water	80	0.01	0.033	$2x10^3$
Fresh water	80	0.5	0.033	0.1
Sea water	80	3000	0.01	10^3
Dry sand	3-5	0.01	0.15	0.01
Saturated sand	20-30	1-10	0.06	0.03-0.3
Limestone	4-8	0.5-2	0.12	0.4-1
Shale	5-15	1-100	0.09	1-100
Silts	5-30	1-100	0.07	1-100
Clay	5-40	2-1000	0.06	1-300
Granite	4-6	0.01-1	0.13	0.01-1
Dry salt	5-6	0.01-1	0.13	0.01-1
Ice	3-4	0.01	0.16	0.01

Table 1: Typical relative permittivity, electrical conductivity, velocity, and attenuation observed in common geological materials

From the values in table 1, a general picture emerges: bulk minerals and aggregates in mixtures are good dielectric insulators. They have a relative permittivity in the range of 3 to 8, are usually insulating, and have virtually zero conductivity. Water is the most polarizable natural occurring material, water in the pore space normally contains ions, and as a result the water conductivity associated with ion mobility is the dominant factor in determining bulk material conductivity (A. Annan, 2005).

In a radargram, the interpretation is usually performed by interface mapping, as the one used in the interpretation of seismograms. If amplitude fidelity has been retained in the radargram, zones of high attenuation can be recognized which represent high conductivity areas such as the ones produced by clay accumulations. However, to identify each band in a radargram as a different lithology would be incorrect, because of the effects of multiples, interference with a previous reflection wavetrain, noise, etc. The processing is simplified by deconvolution, which restores the shape of the downgoing wavetrain so that primary events can be interpreted more easily. Migration is also useful in that diffraction hyperbolae are removed, and correct dips restored (Kearey, Brooks, and Hill, 2013).

4. Seismic

Seismic surveying is the most widely used and well-known geophysical technique. In seismic surveys, seismic energy pulses are reflected from subsurface interfaces and recorded at near-normal incidence at the surface. The travel times are measured and can be converted into estimates of depth to the interfaces (Kearey et al., 2013).

Given the fact that seismic waves are elastic waves propagating through the earth, then the theory of elasticity is used (McQuillin, 1984). The two main concepts in this theory are stress and strain. Stress is defined as force per unit area (equation 4.1) (Sheriff, 1995).

$$\overrightarrow{stress} = \frac{\overrightarrow{F}}{A} \tag{4.1}$$

In a small element of volume inside a stressed body, the stresses acting upon each face of the cube can be solved into components as shown in Figure 5. The subscripts denote the axes (x, y, and z) and σ_{yx} denotes a stress parallel to the y-axis acting upon a surface perpendicular to the x-axis. Identical subscripts, i.e. xx, express normal stresses, if the subscripts are different; the stress is a shearing stress.

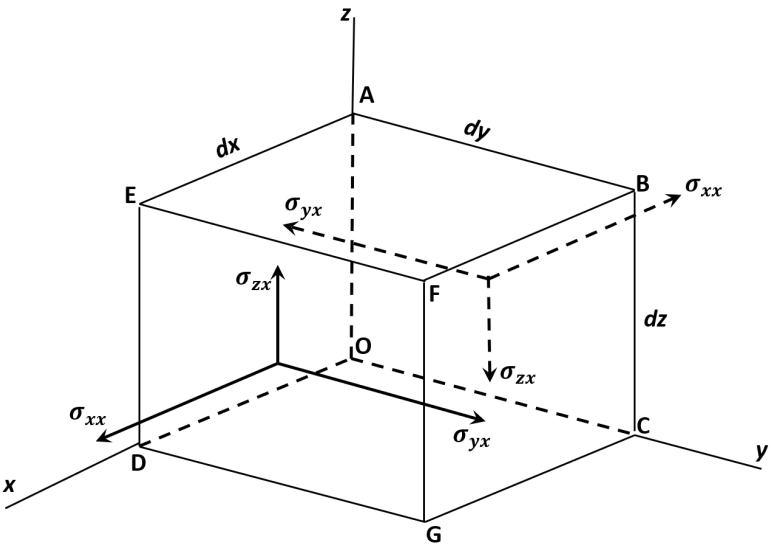

Figure 5: Components of stress on faces perpendicular to x-axis (Sheriff, 1995 p.35)

The medium is in static balance, the stresses must be proportional, this implies σ_{xx},

σ_{yx}, and σ_{zx}, acting on face OABC must be equal and opposite to the stresses shown on face DEFG. This is true for all the remaining faces. In addition, the shearing stresses constitute a couple tending to rotate the element about the z-axis. Because the total moment must be zero, hence, $\sigma_{xy} = \sigma_{yx}$. In general $\sigma_{ij} = \sigma_{ji}$ (Sheriff, 1995).

As discussed in Sheriff, 1995, strain is defined as the changes in shape and dimensions which occur when an elastic body is subjected to stress. Considering the rectangle PQRS shown in Figure 6 in the xy plane. When stresses are applied, P moves to P', and the vector PP' has components u and v. If all other vertices have the same displacement as P, then the rectangle is displaced as a whole with no change in shape. However, if u and v are different for different vertices, the rectangle will suffer changes in shape and size, and strain will exist.

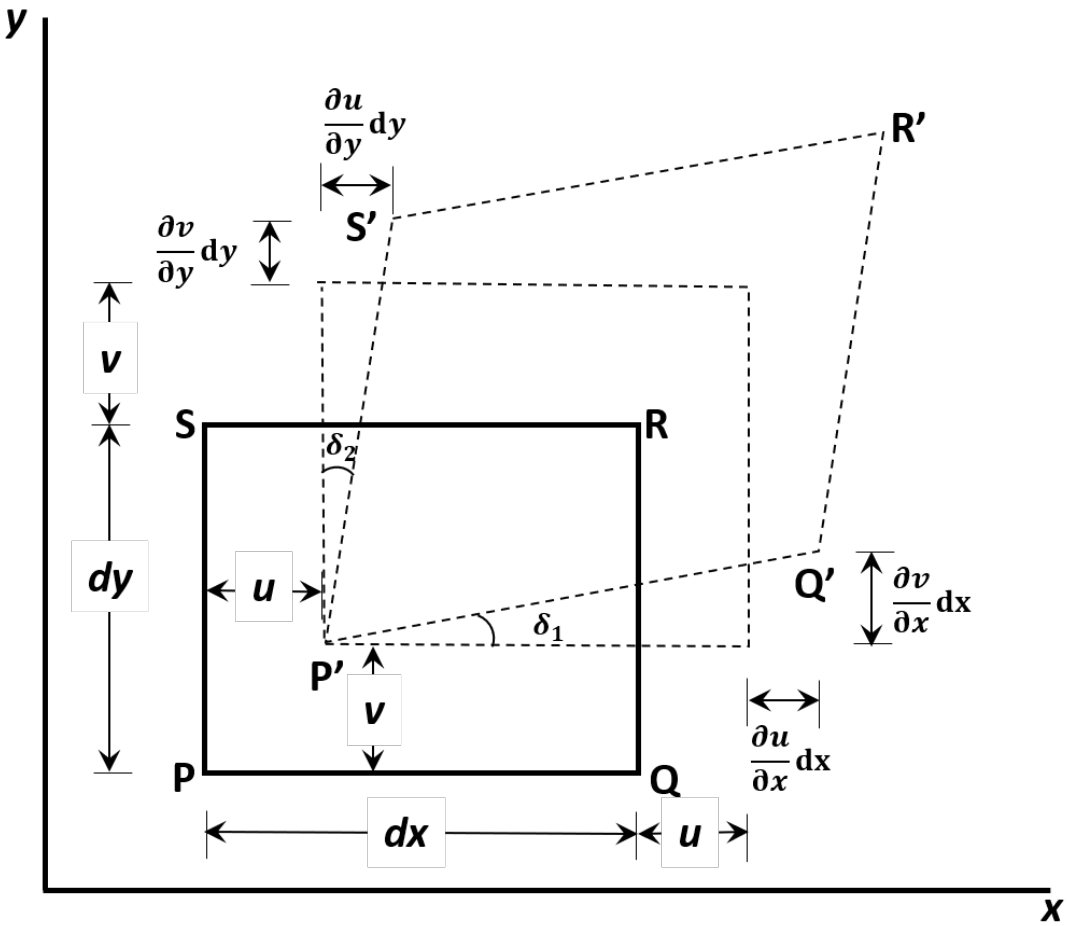

Figure 6: Analysis of two-dimensional strain (Sheriff, 1995 p.36)

Assuming $u = u(x, y)$ and $v = v(x, y)$, then the coordinates of PQRS and P'Q'R'S' are

as follows:

$$\begin{aligned}
P(x,y); &\quad P'(x+u, y+v) \\
Q(x+dx,y); &\quad Q'\left(x+dx+u+\frac{\partial u}{\partial x}dx, y+v+\frac{\partial v}{\partial x}dx\right) \\
S(x,y+dy); &\quad S'\left(x+u+\frac{\partial u}{\partial y}dy, y+dy+v\frac{\partial v}{\partial y}dy\right) \\
R(x+dx,y+dy); &\quad R'\left(x+dx+u+\frac{\partial u}{\partial x}dx+\frac{\partial u}{\partial y}dy, y+dy+v+\frac{\partial v}{\partial x}dx+\frac{\partial v}{\partial y}dy\right)
\end{aligned}$$

The changes in u and v are much smaller than dx and dy, so the differential terms are so small they can be neglected, with this assumption:

* PQ increases in length by the amount $(\partial u/\partial x)$dx and PS by the amount $(\partial v/\partial y)$dy, hence $\partial u/\partial x$ and $\partial v/\partial y$ are the fractional increases in length
* The angles δ_1 and δ_2 are equal to $\partial v/\partial x$ and $\partial u/\partial y$, respectively
* The right angle at P decreases by the amount $\delta_1 + \delta_2 = \partial v/\partial x + \partial u/\partial y$
* The rectangle as a whole has been rotated counterclockwise through the angle $(\delta_1 - \delta_2)/2 = (\partial v/\partial x - \partial u/\partial y)/2$

Extending the analysis to three dimensions, the components of displacement (u,v,w) for the point P(x,y,z) is defined as:

$$\left.\begin{aligned}
\varepsilon_{xx} &= \frac{\partial u}{\partial x} \\
\varepsilon_{yy} &= \frac{\partial v}{\partial y} \\
\varepsilon_{zz} &= \frac{\partial w}{\partial z}
\end{aligned}\right\} \quad \text{Normal strains}$$

$$\left.\begin{aligned}
\varepsilon_{xy} = \varepsilon_{yx} &= \frac{\partial v}{\partial x} + \frac{\partial u}{\partial y} \\
\varepsilon_{yz} = \varepsilon_{zy} &= \frac{\partial w}{\partial y} + \frac{\partial v}{\partial z} \\
\varepsilon_{zx} = \varepsilon_{xz} &= \frac{\partial u}{\partial z} + \frac{\partial w}{\partial x}
\end{aligned}\right\} \quad \text{Shearing strains}$$

In addition, the rotation is defined by:

$$\left.\begin{aligned} \theta_x &= \frac{\partial w/\partial y - \partial v/\partial z}{2} \\ \theta_y &= \frac{\partial u/\partial z - \partial w/\partial x}{2} \\ \theta_z &= \frac{\partial v/\partial x - \partial u/\partial y}{2} \end{aligned}\right\}$$

The change in volume resulting from stress is called dilatation and it is represented by Δ. Because the original volume of the cube was dxdydz, the change in volume per unit volume is:

$$\Delta = \varepsilon_{xx} + \varepsilon_{yy} + \varepsilon_{zz} = \frac{\partial u}{\partial x} + \frac{\partial v}{\partial y} + \frac{\partial w}{\partial z} \tag{4.2}$$

The relationship between stress and strain is given by Hooke's law, which states that a given strain is directly proportional to the stress producing it. When the medium is isotropic, it can be expressed in the following form:

$$\sigma_{ii} = \lambda\Delta + 2\mu\varepsilon_{ii} \qquad (i = x, y, z) \tag{4.3}$$

$$\sigma_{ij} = 2\mu\varepsilon_{ij} \qquad (i, j = x, y, z; i \neq j) \tag{4.4}$$

The quantities λ and μ are known as Lamé's constants.

The elastic moduli and densities of the materials through which they pass determine the propagation velocities of seismic pulses.

By virtue of their various compositions, textures, porosities and contained pore fluids, rocks differ in their elastic moduli and densities, and, hence, in their seismic velocities. Typical values for compressional waves velocity values and ranges for a variety of materials is given in table 2.

At an interface between two rock layers, there is generally a change of propagation velocity resulting from the difference in physical properties of the two layers. At such interface,

Material	V_P km/s
Dry sand	0.2-1.0
Saturated sand	1.5-2.0
Clay	1.0-2.5
Glacial till	3.5-4.0
Sandstone	2.0-6.0
Limestone	2.0-6.0
Dolomite	2.5-6.5
Granite	5.5-6.0
Gabbro	6.5-7.0
Air	0.3
Water	1.4-1.5
Ice	3.4

Table 2: Compressional wave velocities in Earth materials (Kearey, Brooks, and Hill, 2013)

the energy within an incident seismic pulse is partitioned into transmitted and reflected pulses. The relative amplitudes of these pulses depend on the velocities and densities of both layers, and the angle of incidence on the interface as shown in Figure 7 (Kearey et al., 2013).

In the case of seismic exploration, if a movement is generated in point A in the surface, one of the multiple trajectories will arrive to point B. This generates a wave reflected with an angle r, equal to the incidence angle i, which will propagate towards the surface to be detected by a geophone placed in point C, at an X distance from the impact point A.

The total time of the trajectory is defined by the time it took to go from A to B and B to C, with an average propagation velocity V, as shown in equation 4.5

$$T_{BC} = T_{AB} + T_{BC} = \frac{AB + BC}{V} \tag{4.5}$$

In the case of parallel layers, AB=BC, so equation 4.5 can be rewritten as $T = 2T_{AB} = \frac{2_{AB}}{V}$ and $AB = \sqrt{\frac{X^2}{4} + Z^2}$, combining these two equations, we get:

$$Z = \frac{1}{2}\Big(T^2V^2 - X^2\Big)^{\frac{1}{2}} \tag{4.6}$$

By plotting equation 4.6, the travel time curve is a parabola, which is tangent to the lines

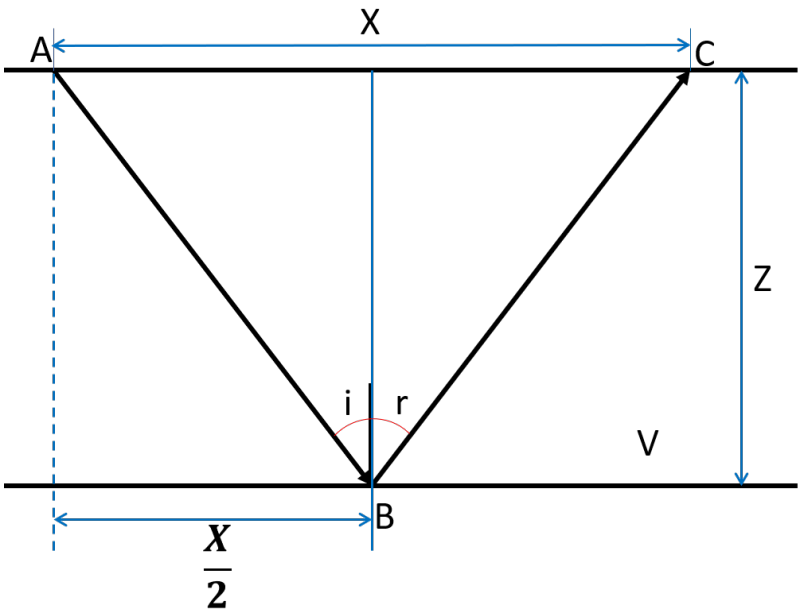

Figure 7: Representation of Snell's law, wavefront source is point A, B is the point of incidence between the two layers, and C is the point where the reflected wave reaches the surface. Incidence angle: i, reflection angle: r.

representing the velocities of both layers as shown in Figure 9.

Propagation velocities cannot be obtained directly using the values of the travel time of the reflected waves that have been registered. However, if the squared values for time and distance are plotted for each detected point, then a straight line is obtained (del Valle Toledo, 1984).

$$T^2 = \frac{X^2 + 4Z^2}{V^2} \tag{4.7}$$

If we plot T^2 against X^2, instead of T vs X then:

$$y = \frac{x}{V^2} + \frac{4Z^2}{V^2} \tag{4.8}$$

This takes the form $y = mx + b$ where $m = \frac{1}{V^2}$ and $T_0 = \frac{4Z^2}{V^2}$

Equation 4.7 is true for any number of layers; however, in real situations it is difficult to have the proper amount of points defining properly the line. Nevertheless, this would require measuring time for big distances, which in the seismic reflection method is not

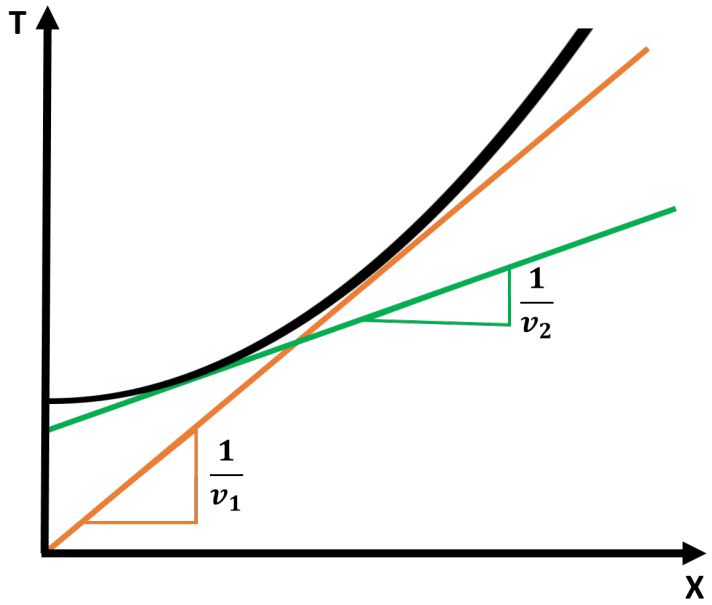

Figure 8: T vs X plot, parabola is tangent to the lines representing the inverse of the velocities of the two layers.

convenient (del Valle Toledo, 1984).

The gathered data from a seismic study is displayed in a seismogram, which represents the combined response of the layered ground and the recording system to a seismic pulse, in our case, to the sledgehammer shots (Kearey et al., 2013).

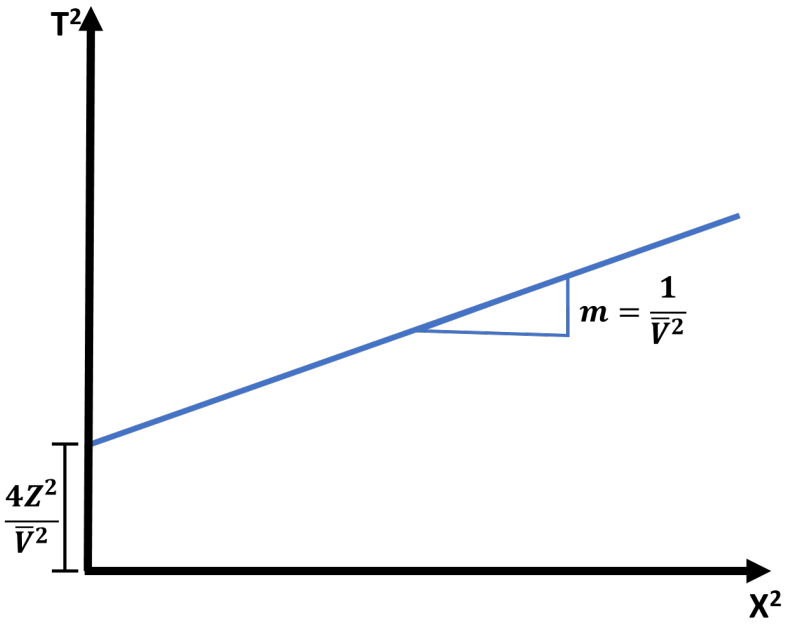

Figure 9: T2 vs X2 plot

5. Data acquisition

The data acquisition was performed in three different sites in the Jæren area, marked in Figure 10

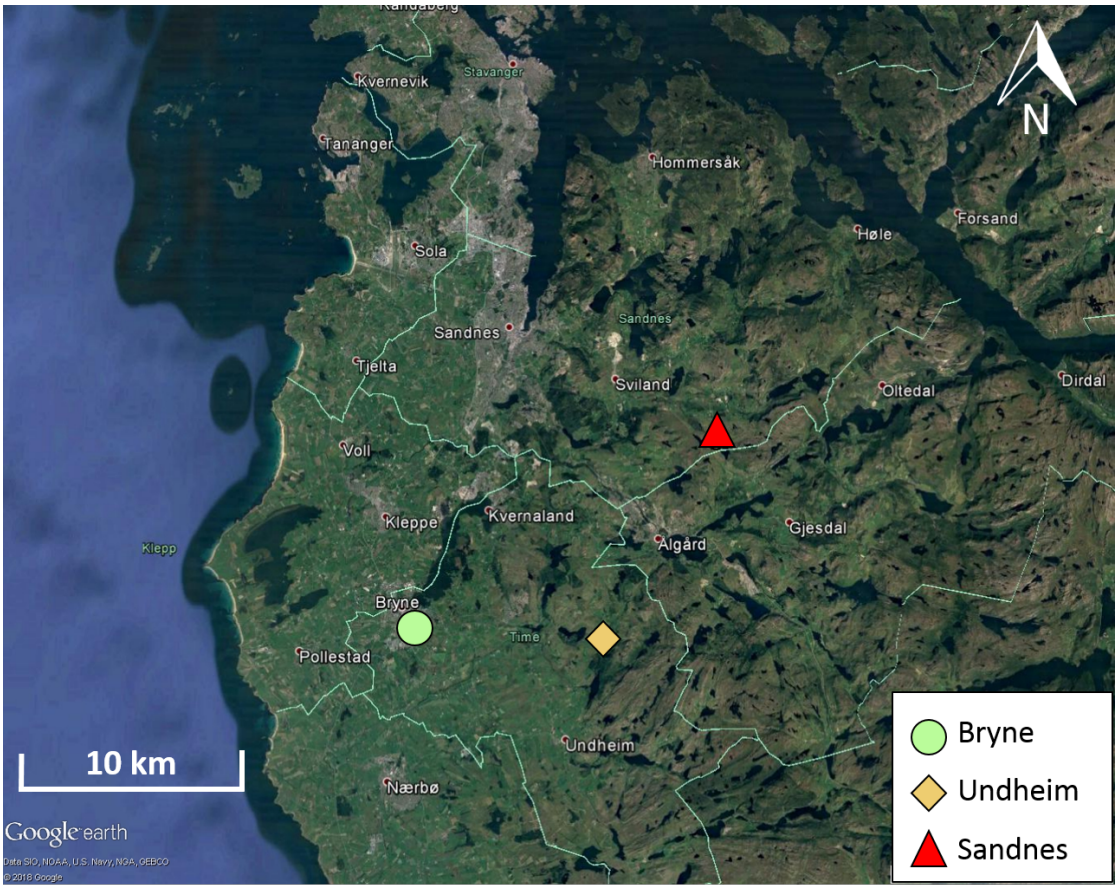

Figure 10: Location of area of study, showing explored sites.

In the Undheim site both GPR and seismic data were acquired. In the other two sites, Bryne and Sandnes, only GPR acquisition was performed. The acquisition of GPR data was performed on two different days, and the reflection seismic data acquisition on a third day.

GPR data acquisition was performed with a Malå GX HDR system equipped with a 80MHz antenna mounted on a rough terrain cart. A 30 cm measuring wheel acted as a trigging device instructing the antenna to collect traces at fixed intervals and was used for length measurement (Singh, Kulkarni, and Mishra, 2010). The equipment is shown in Figure 11.

a) b)

Figure 11: GPR equipment: a) 80Mhz antenna and b) console

Given the non-destructive character of GPR, it was possible to perform the acquisition in different weather conditions, such as snow and frozen ground.

The seismic acquisition was performed with a RT2 system from Wireless Seismic, with 24 three-component geophones (Figure 12, left). A line interface unit (Figure 12, right) collects the real-time seismic data and it is sent to the central recording system. The source used was manual, stacking ten sledgehammer strikes to enhance the seismic signal.

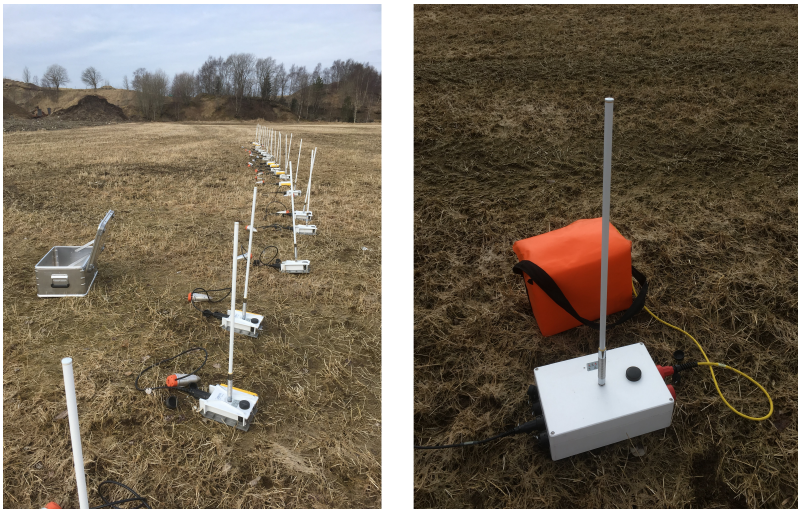

Figure 12: Seismic equipment, left: Geophones and right: Line interface unit

The restrictions for the seismic acquisition were diverse:

* Location: next to an active quarry, to avoid the noise generated from the machinery

it had to be done in a weekend.

* Weather: the geophones are highly sensitive to ambient noise; it had to be performed without rain.

* Temperature: the geophones must be grounded, this restriction implies digging a hole and compressing the soil around the geophone to make sure it stays in place. With freezing temperature, this was not an easy task, so special equipment had to be used (Figure 13).

* Number of lines: originally the acquisition of two or more seismic lines was planned, however, given all the previous restrictions only one day was suitable for acquisition, cutting short the chances of performing more seismic studies.

Figure 13: Geophone grounding preparation.

The seismic acquisition was performed in the array shown in Figure 14. This seismic line is placed exactly in the same location as one of the GPR lines to perform the comparison of data. The blue triangles represent the 24 geophones, and the red crosses mark the nine shot points.

As the geophones acquire three components -horizontal, vertical, and transverse- the data must be separated into these components for its processing.

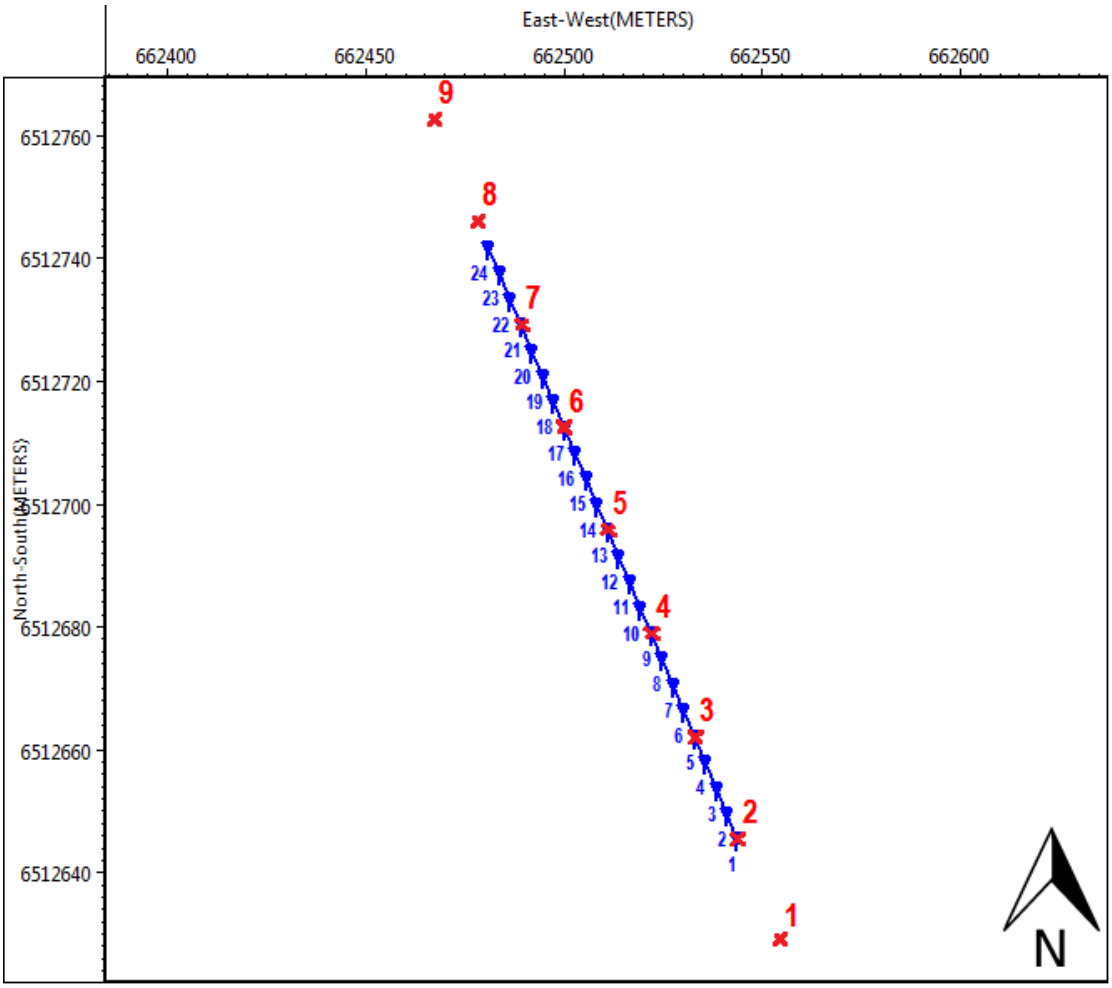

Figure 14: Seismic acquisition array, blue triangles represent the geophones (receivers) and the red cross represents the shot points

The geological maps used in the next sections were retrieved from Norges Geologiske Undelsøkelse, 2018.

5.1. Undheim site

The location of the Undheim site was shown in Figure 10. In Figure 15 the location of the acquired GPR lines with geology is marked.

Undheim site is located next to the sand quarry Sæland massetak in Time kommune. The composition of the material extracted in this quarry varies, but it is mainly composed of sand with some gravel layers, especially in the top. At the bottom, it is possible to encounter unsorted material. In Figure 15 it is possible to observe the geological

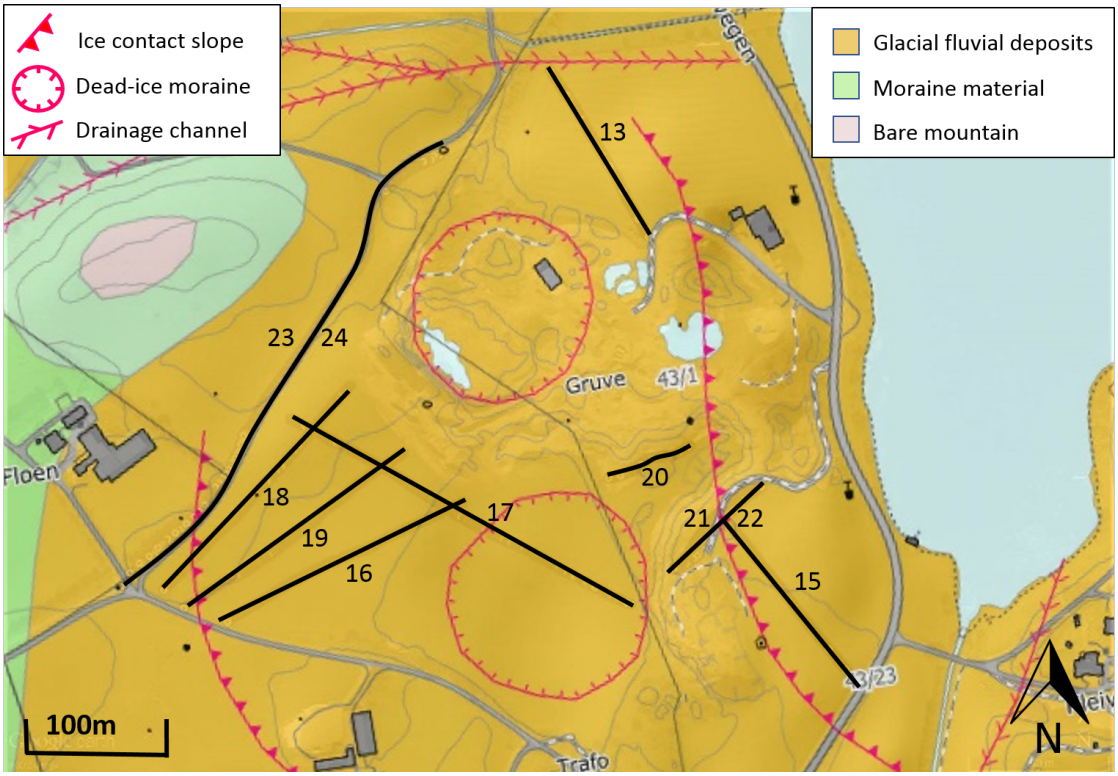

Figure 15: Geology of Undheim site, with acquired GPR lines marked.

composition of the area, which is mainly glaciofluvial deposits in the area where the GPR and seismic data were acquired. It is also possible to observe glacial structures such as dead ice moraine ice contact slopes.

The acquisition was performed in three stages:

* Day 1: acquisition of 7 GPR lines (13, 15, 16, 17, 18, 19, 20).
* Day 2: acquisition of 4 GPR lines (21, 22, 23, 24).

A preliminary interpretation of the GPR lines was performed to determine the best location to acquire seismic data.

* Day 3: Reflection seismic acquisition on the same location as GPR line 13

At the beginning of the line, there was a pile of gravel where the initial shot point was supposed to be located. As such, it was not possible to place the steel plate (for the hammer strikes), so it had to be closer than planned. At the end of the line, as mentioned

before, a drainage channel was on the way, so it was necessary to move the shot point closer to the last receiver. In Figure 15 at the North of line 13 the channel can be observed. This channel introduced some noise to the seismic data; the processing steps to remove this noise will be discussed deeper in the next chapter.

5.2. Bryne site

In Figure 16 it is possible to see the geology of the Bryne site, with the acquired GPR lines marked.

The geology of the area shows mainly moraine material, and at the North of the site, it is possible to see the remains of a swamp.

Figure 16: Geology of Bryne site, with acquired GPR lines marked.

As a quality control measure, the first acquired line was recorded NW-SE and afterwards

SE-NW. The three remaining GPR lines were acquired in a single run.

As with the previous site discussed in subsection 5.1 data was recorded on day 1 of acquisition. This was done with freezing conditions and snow covering the field, which, as mentioned before, is not a problem for GPR acquisition.

5.3. Sandnes site

The third site, Sandnes, is composed of moraine material as seen in Figure 17. This site, as well as Undheim site, is also located next to an active sand quarry.

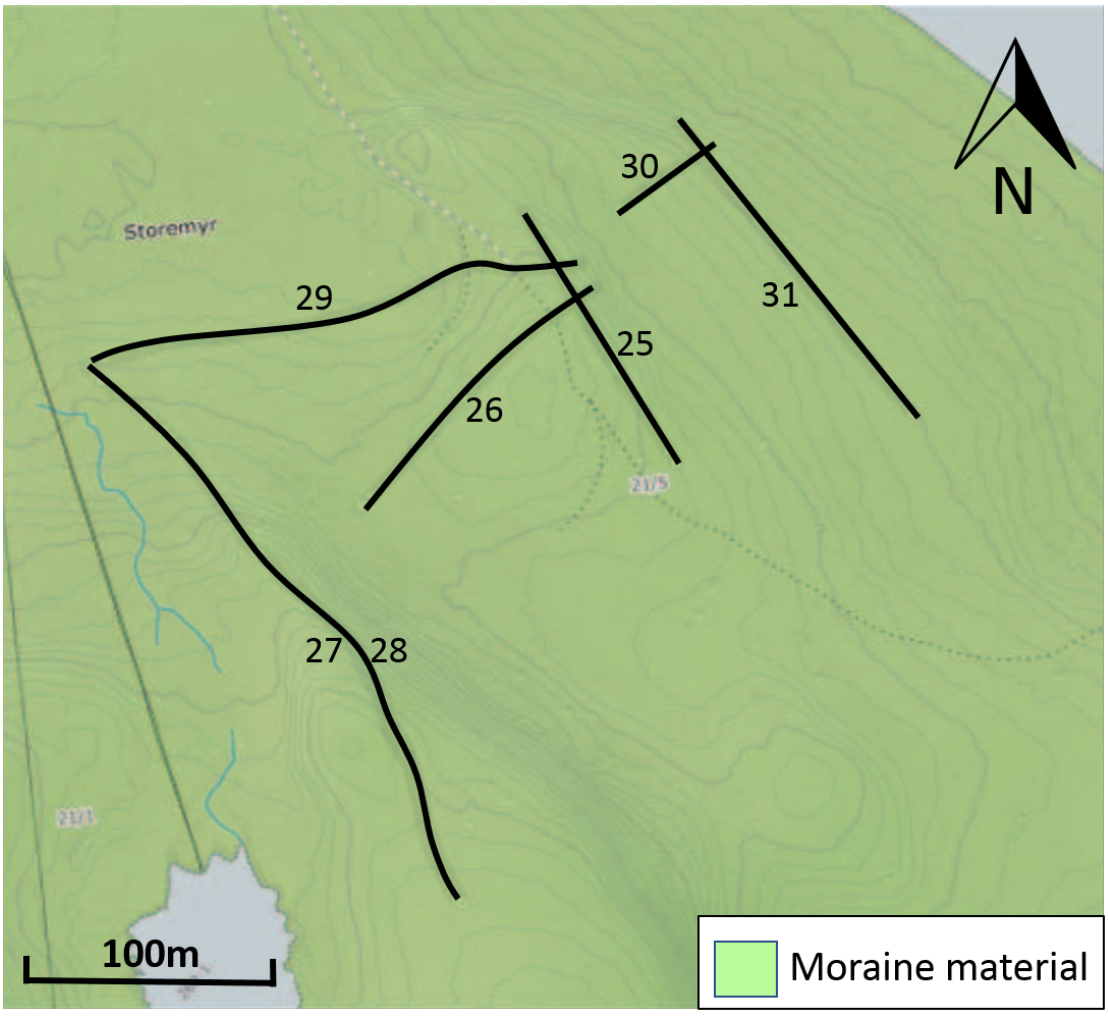

Figure 17: Geology of Sandnes site, with acquired GPR lines marked.

Seven GPR lines were acquired in day 2 of the acquisition. Line 27 and 28 were acquired in the same location going in opposite directions. The area was covered with snow, which

made it difficult to keep the acquisition in straight lines; low visibility and large boulders hidden in the snow forced the lines to deviate.

The main goal for this site was to determine the depth location of the basement.

As mentioned in chapter 2, in moraine material deposits it is possible to find sand with layers of unsorted material. The basement in this area is not deep, given that it is possible to observe it in the nearby mountains.

According to Norges Geologiske Undersøkelse (NGU, the Geological Survey of Norway), the basement in this area is composed of metamorphic rocks.

6. Dataset

6.1. Ground penetrating radar data

The GPR acquisition generates several output files, but the most important ones for this work are the *.rd3 files which contain the raw GPR data, and the *.cor files which contain the GPS position of each acquired point as well as the elevation data which will be used for topographical correction. In table 3, it is possible to see a summary of the acquired lines in each site and the length of each one of them.

Undheim		Bryne		Sandnes	
GPR line	Length (m)	GPR line	Length (m)	GPR line	Length (m)
13	143	8	211	25	121
15	151	9	209	26	127
16	190	10	216	27	134
17	279	11	177	28	263
18	198	12	220	29	205
19	191			30	47
20	63			31	155
21	82				
22	88				
23	369				
24	385				

Table 3: GPR lines in each location showing length

The raw data as shown in Figure 18 shows that it is not possible to perform an interpretation. However, it is possible to see the quality of the acquired data with an automatic gain control filter to enhance the acquired data. The processing steps will be discussed in chapter 7.

6.2. Seismic

One seismic line was acquired in Undheim, in the same location as GPR line 13. The initial and final shot points presented problems, so they had to be acquired at a different distance than the rest.

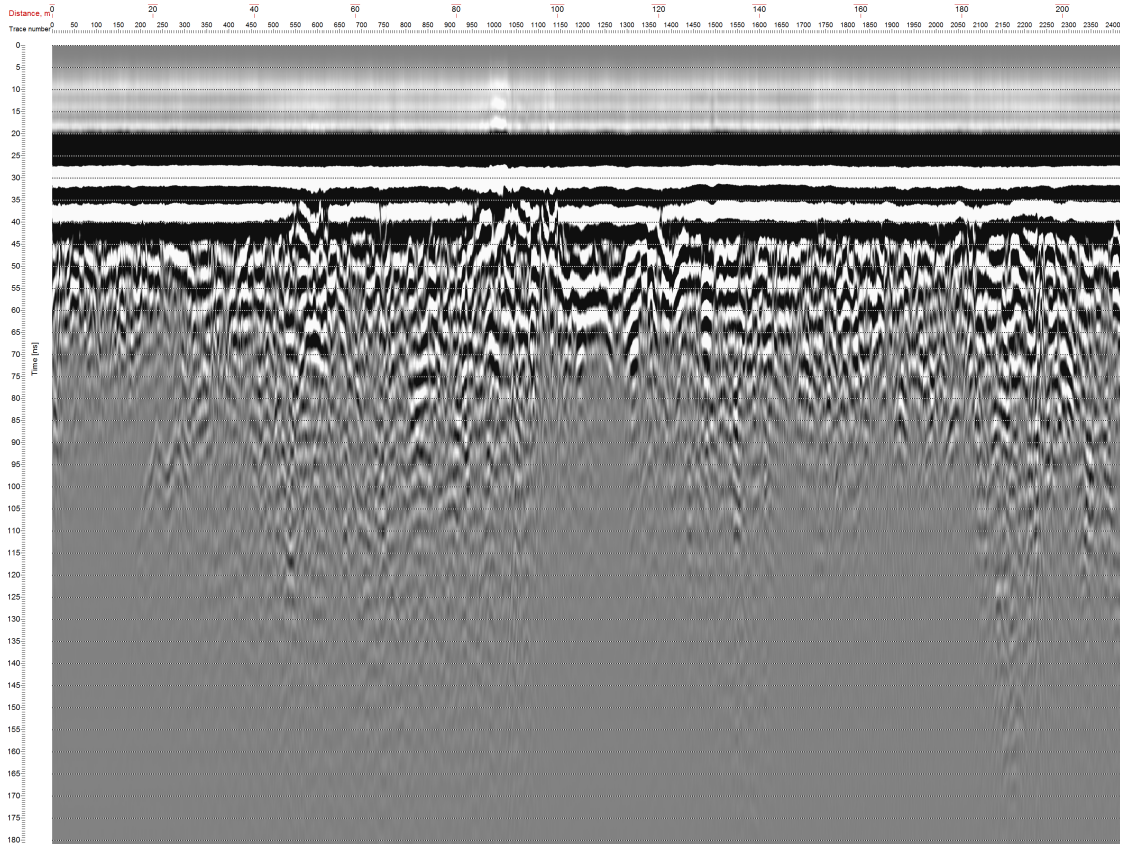

Figure 18: Raw GPR data in line 8

As mentioned in chapter 5, the used geophones acquired three components, so the output file contains 72 traces with information: one trace x three components x 24 channels= 72 traces. This seismogram has to be divided into three seismograms, one per each component. The raw data for the vertical component is shown in Figure 19.

Another thing to consider is that during the acquisition, nine shot points were recorded. So once again, the data has to be divided every 24 geophones to have the information of the first arrival of each shot point. Figure 20, shows the seismogram for the 24 channels during the first shot, in the vertical component.

The recording is 2 seconds long; however, since only the first arrival (P-wave) will be used for the modeling, then it is possible to work just with one second of the data.

The seismic shown in Figure 20 has been windowed, filtered and normalized, then it has been loaded in Matlab. This is done to make the picking of the first arrival of the wave easier. In addition, it can be observed on the upper right corner of the seismogram that there is a big amount of noise, most probably related to the drainage channel, but the

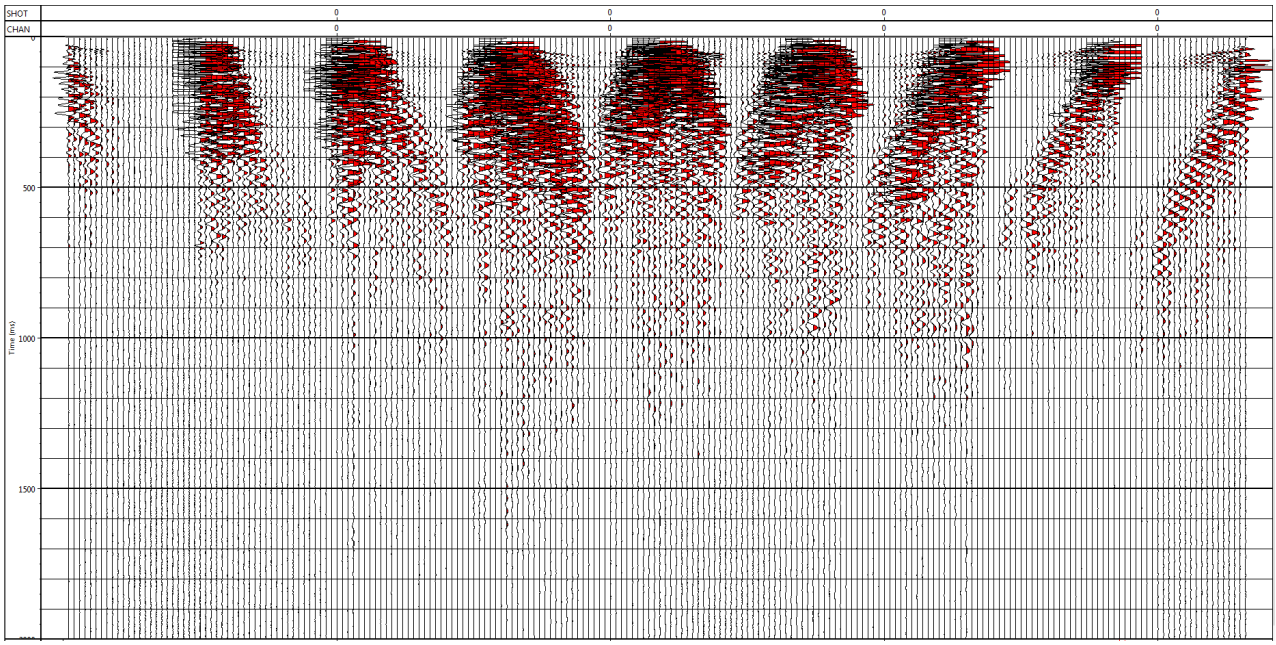

Figure 19: Seismic raw data, vertical component

first arrival can be observed below the noise since it has a strong response compared to the noise.

As one of the objectives of this work is to join and compare the results of both geophysical methods, it is important to have the right location of both lines to be able to merge and obtain combined results.

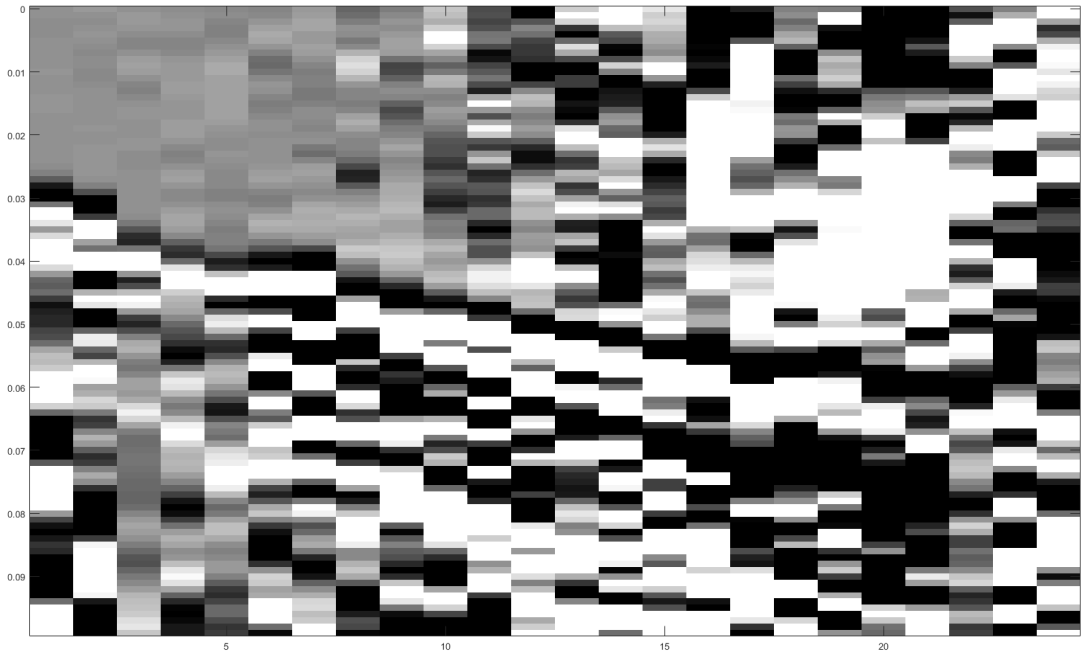

Figure 20: Seismic data for source 1, vertical component

7. Processing

7.1. Ground penetrating radar

The raw data is loaded into the software RadExplorer v. 1.42 by Malå GeoScience. The processing steps are performed in time domain, and the data is not related directly to depth. To convert the section to a depth scale an accurate estimate of the average subsurface velocity must be obtained through hyperbolic velocity analysis (Jol, 2009).

The processing steps for GPR data are summarized in Figure 21

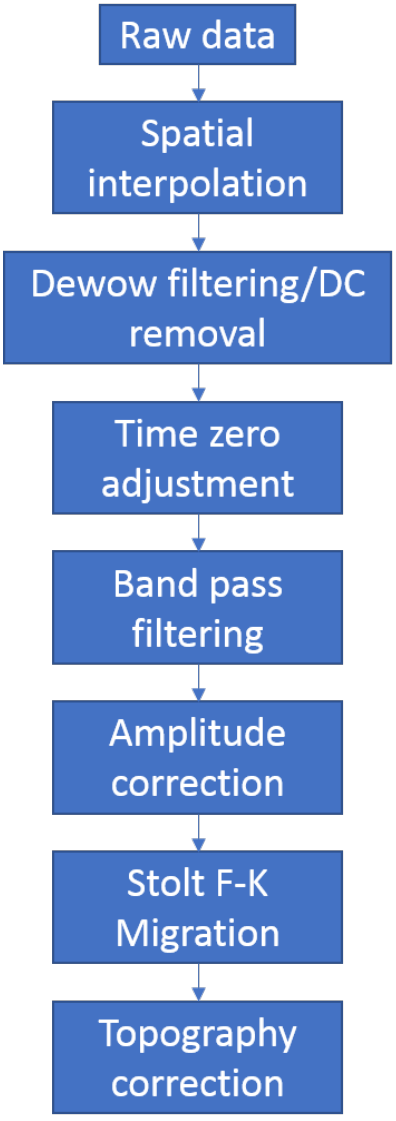

Figure 21: GPR processing workflow.

Incoherent, noisy, or missed traces can be caused by external noise sources, equipment failure, or by an irregularity on the ground, causing the wheel to disconnect from the ground; in most cases only the occassional trace is corrupted and it can be fixed with an interpolation between traces. The processing routine in the software that was used is called spatial interpolation (Jol, 2009).

The next step is the removal of the initial DC signal component, and subsequent decay of "wow" or low frequency signal trend present in the data. "Wow" is caused by the saturation of the recorded signal by early arrivals and/or inductive coupling effects and requires the subtraction of the DC bias from the signal and the application of an optimized, low-cut, or median filter for effective correction (Jol, 2009 and P. Annan, 2003). The processing routine is called DC removal.

Time zero adjustment is done to avoid "jumps" in the wavelet first arrival time. This influences the position of the ground interface in the section. Therefore, traces require adjusting to a common time zero position before continuing with the processing steps. This was achieved by using the air wave first break point as an anchor point for the rest of the line (Jol, 2009).

Band-pass filtering is applied to remove cultural and system noise, such as the EM waves generated for radio frequencies, mobile phones, etc. It is also used to improve the visual quality of the data. The rule of thumb is to set the pass region symmetrically around the peak signal frequency with a bandwidth that is equal to 1.5 times its value, so the values used for the band-pass filter of the 80MHz antenna were between 20-140MHz (A. Annan, 2005 and Jol, 2009). Up to this point, the processing is considered basic and there is no significant improvement in the data quality.

The GPR signal has to travel through different media, which causes it to lose energy, due to scattering attenuation. To reduce the impact of this, an amplitude correction is applied to the data. Figure 22 shows the comparison between raw data and processed data with all the previous steps up to amplitude correction.

Migration is a spatial deconvolution, the goal of which is to reconstruct the radar reflectivity distribution of the subsurface. To perform this task, it is necessary to have knowledge of the velocity structure, which is calculated with hyperbolic matching

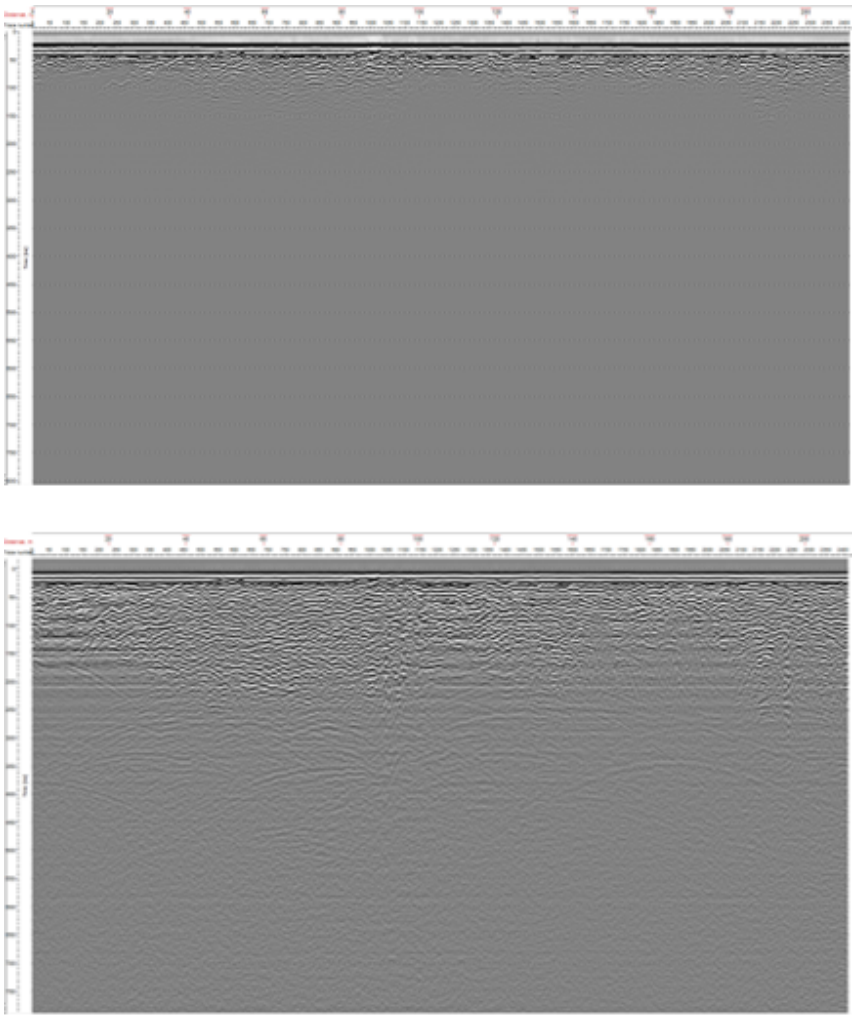

Figure 22: GPR data processing in line 8, top: raw data and bottom: processed data with amplitude correction

(A. Annan, 2005)

Hyperbolic matching can be performed on any section that contains diffraction or reflection hyperbola and is achieved by matching the ideal form of a velocity-specified hyperbolic function to the form of the observed data (Jol, 2009). The hyperbolic matching can be observed in Figure 23. It is also possible to observe that there are several locations where a hyperbola can be fitted, each one with different velocities. This situation can be attributed to the different layers or structures being analyzed. These velocities will be used in the migration step, since this is an interactive model and it is necessary to optimize the image by adjusting the background velocity.

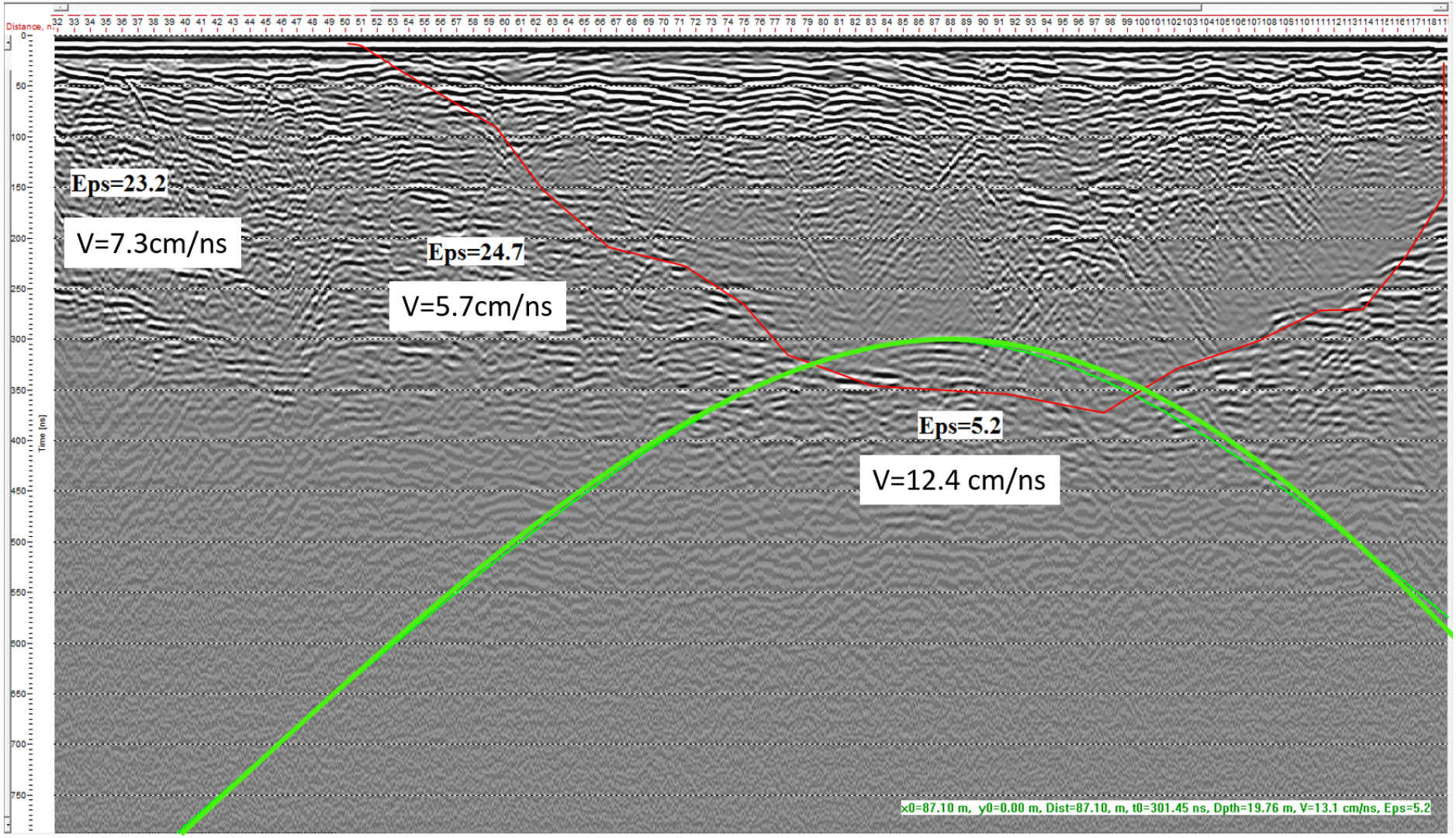

Figure 23: Hyperbolic matching performed in GPR line 13

In the software, the migration process used is Stolt F-K migration, and a migration velocity has to be entered. By changing the velocity values to the ones obtained with hyperbolic fitting, the migration is performed. However, only one value can be used, and some are not producing a reliable result. As an analog of seismic migration, some of the velocities produce ”smiles” which are attributed to overmigration. This makes trying to obtain a good image without artifacts such as ”smiles” or ”frowns” an iterative process (Zhu, Lines, and Gray, 1998); and the goal of this process is to collapse the diffraction hyperbolae to a point source and reposition dipping reflectors into their correct location (Jol, 2009).

A topographic correction is required to position the data in its correct spatial context; this is performed with a simple velocity correction that acts in a vertical sense. The obtained topography data has to be put into a format accepted by the software, a sample of one of these is shown in Appendix A1. After applying the topographic correction, the data appears as shown in Figure 24

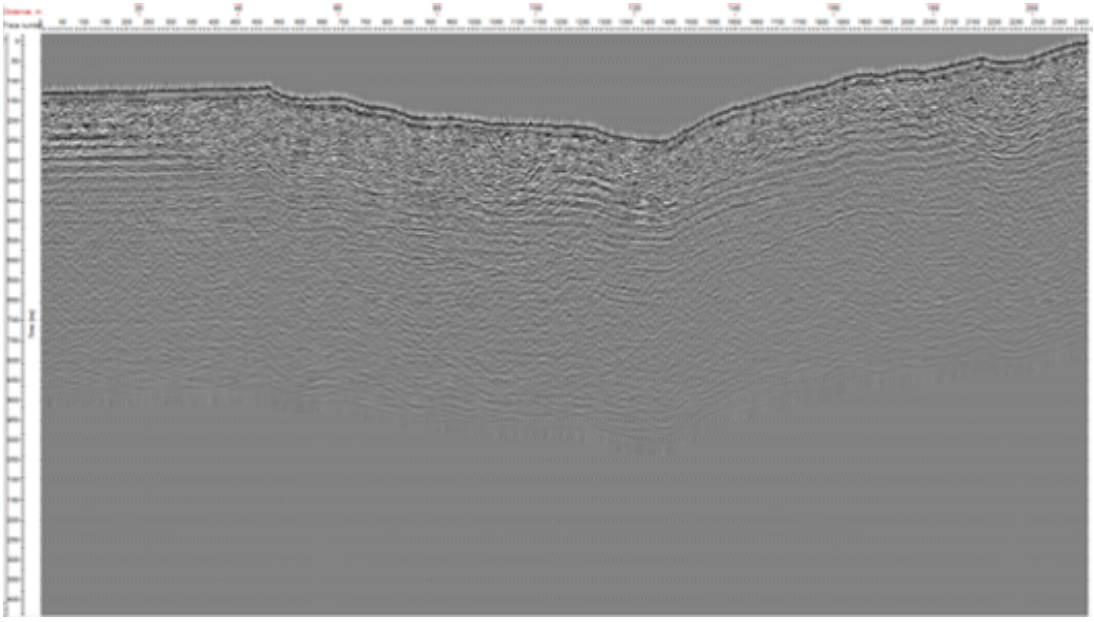

Figure 24: GPR processed data with topographic correction

Once all the data has been filtered, enhanced and corrected, the next step is the depth conversion. To perform this step, it is necessary to interpret the structures observed in the radargram. This process is performed in the same way as in seismic interpretation. To assign the electromagnetic wave velocities of the different layers, several sources are used: velocities obtained from the hyperbolic matching, velocity used for migration, and

geological information of the area combined with velocity tables from the literature. In Figure 25, a time radargram is interpreted showing the observed layers.

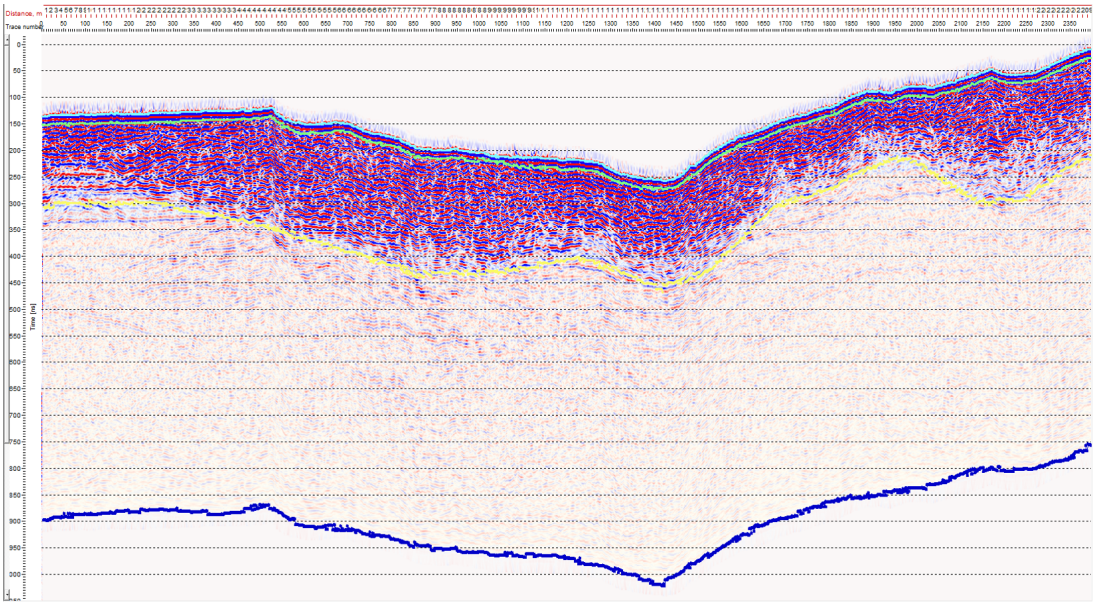

Figure 25: GPR interpretation on line 8

The velocity model works with a layer cake model, so it is necessary to create the layers in the editor by assigning them between interpreted horizons and a velocity is assigned to each layer. The model is then converted from two-way travel time to depth (Malå GeoScience, 2005).

All the satellite images used in the next sections were retrieved from Google, n.d.

As a first approach for the interpretation, the layers were depth converted. After this process, the GPR lines in depth were exported into a modeling software where the main geological structures will be interpreted.

For the depth conversion, a general model is defined with the velocities of the encountered layers. The site in Undheim presents a cross-section, as seen in Figure 4, where it is possible to see the composition of the layers, by combining that data with the information from Direktoratet for mineralforvaltning, 2014, it is possible to define a tentative geology for the area.

Figure 26 shows the location of the acquired GPR lines and the general model used in this site. The main geological layers observed are a thin layer of soil, a massive sand body with intrusions, which have been identified as moraine material, or dead ice, and finally

a metamorphic basement.

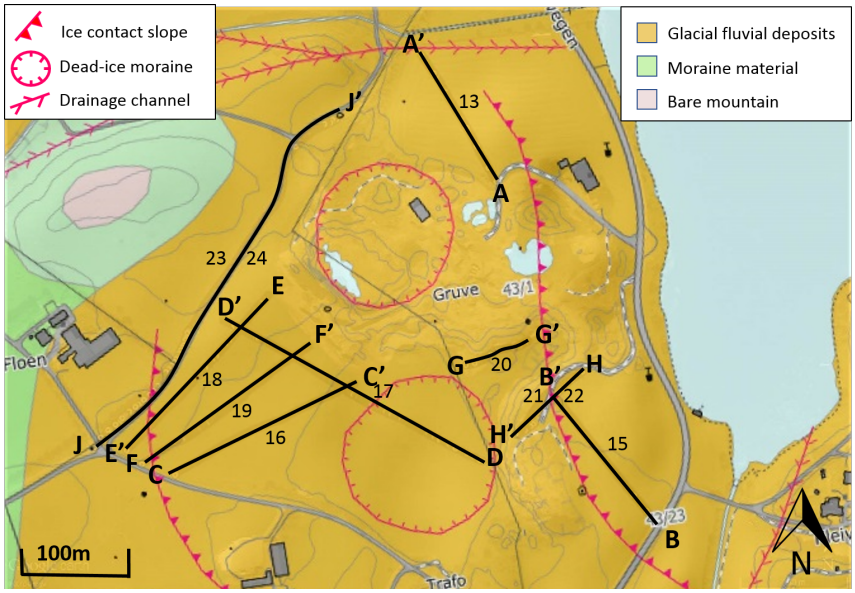

(a) Location map

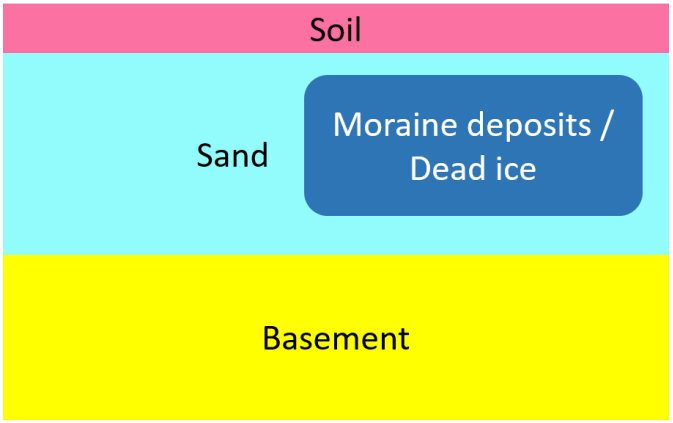

(b) General model

Figure 26: (a) Location of Undheim lines (b) General model in Undheim

In the second site, Bryne, the same procedure was followed; however, the only information available is about the surface geology and the basement, so some assumptions were made to generate the general model used for depth conversion. Figure 27 shows the location of the lines and the general model used. The geology includes a layer of soil, a layer of clay, swamp deposits, and a metamorphic basement.

In the last site, Sandnes, the geological information is scarce, so assumptions had to be done with the velocities obtained from hyperbolic matching. In Figure 28, the location of the lines is marked and the general geological model is shown. A high velocity body is observed in most of the acquired lines, but it not possible to define the type of rock just

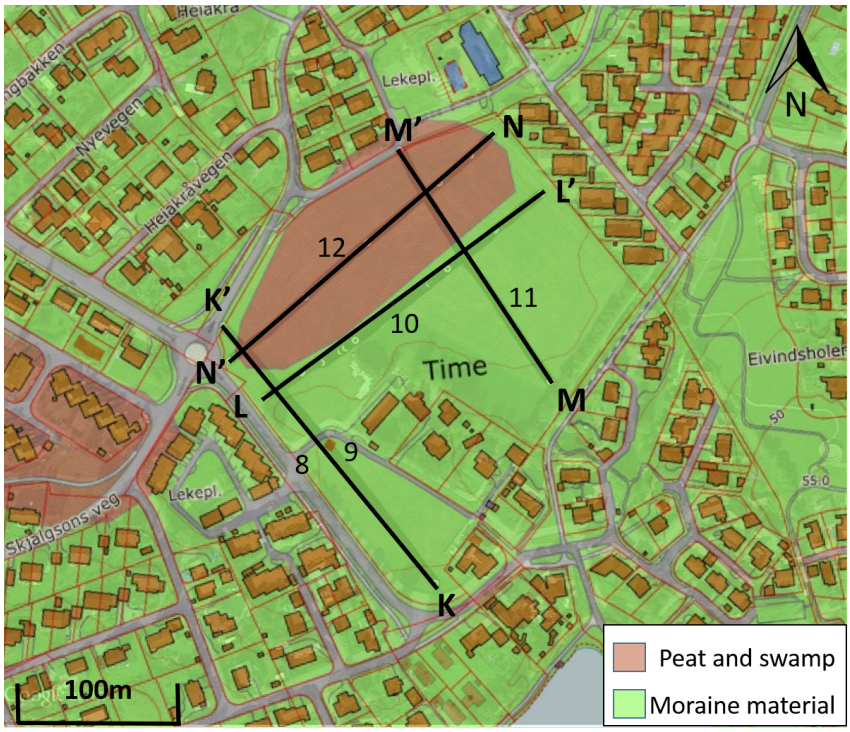

(a) Location map

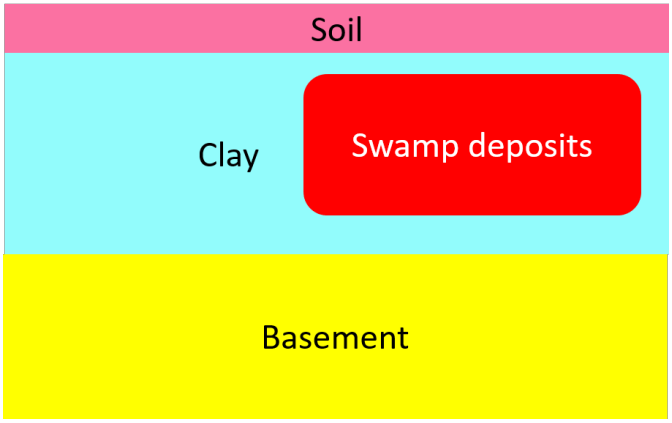

(b) General model

Figure 27: (a) Location of Bryne lines (b) General model in Bryne

with this information. Using tables an assumption on the lithology can be made, but this will be discussed in chapter 8.

In some of the GPR lines, the edge of the basement was not clear, so some seismic attributes were applied in order to enhance this boundary (Tronicke and Böniger, 2013). The attribute that provides the best result was Envelope (Reflection strength). This attribute represents the instantaneous energy of the signal and is proportional in its magnitude to the reflection coefficient. This attribute is mostly used to highlight discontinuities, faults, or as in this case changes in lithology (Koson, Chenrai, and

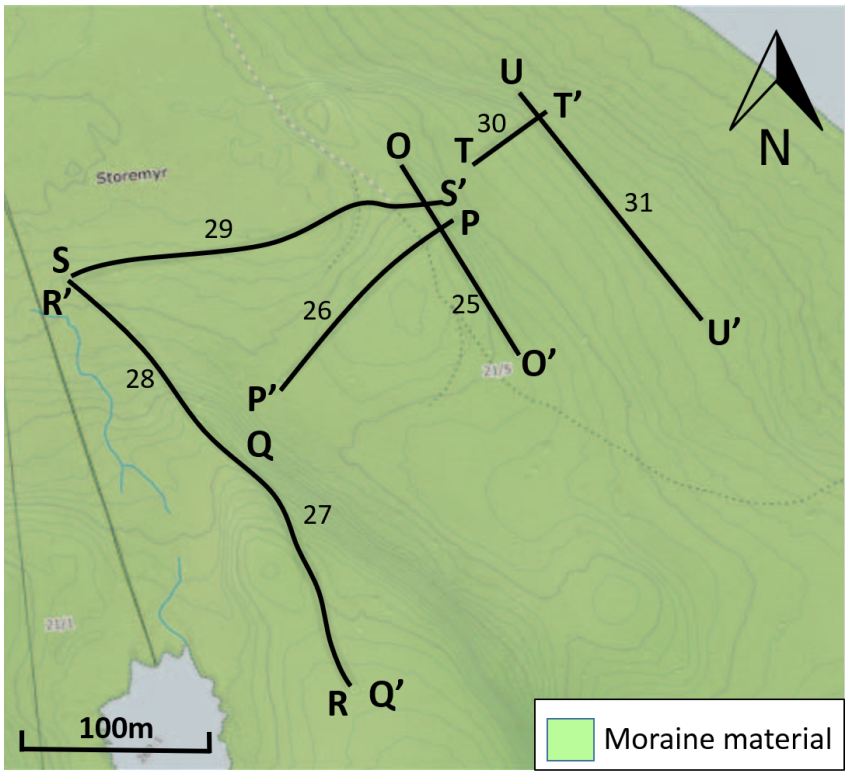

(a) Location map

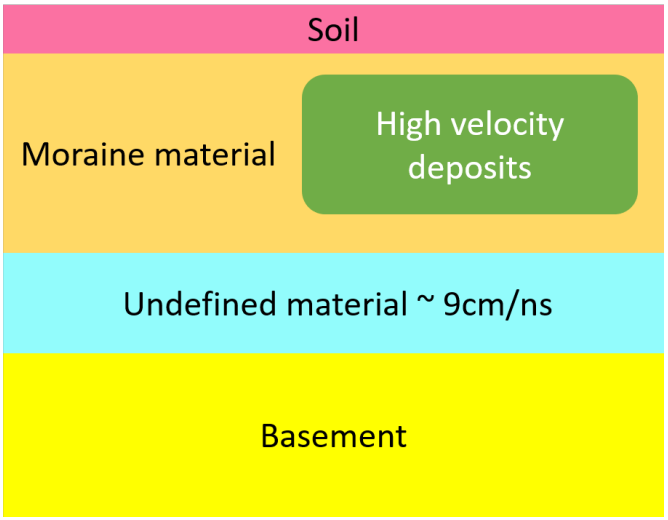

(b) General model

Figure 28: (a) Location of Sandnes lines (b) General model in Sandnes

Choowong, 2014).

7.2. Seismic

In this work, refraction data is used. This is due to the wavelength of the reflected waves being too large.

The first step for the seismic processing is to load the raw data in Matlab. The second step is picking the first arrival of the seismic wave (P-wave) in the seismogram, as shown in Figure 29.

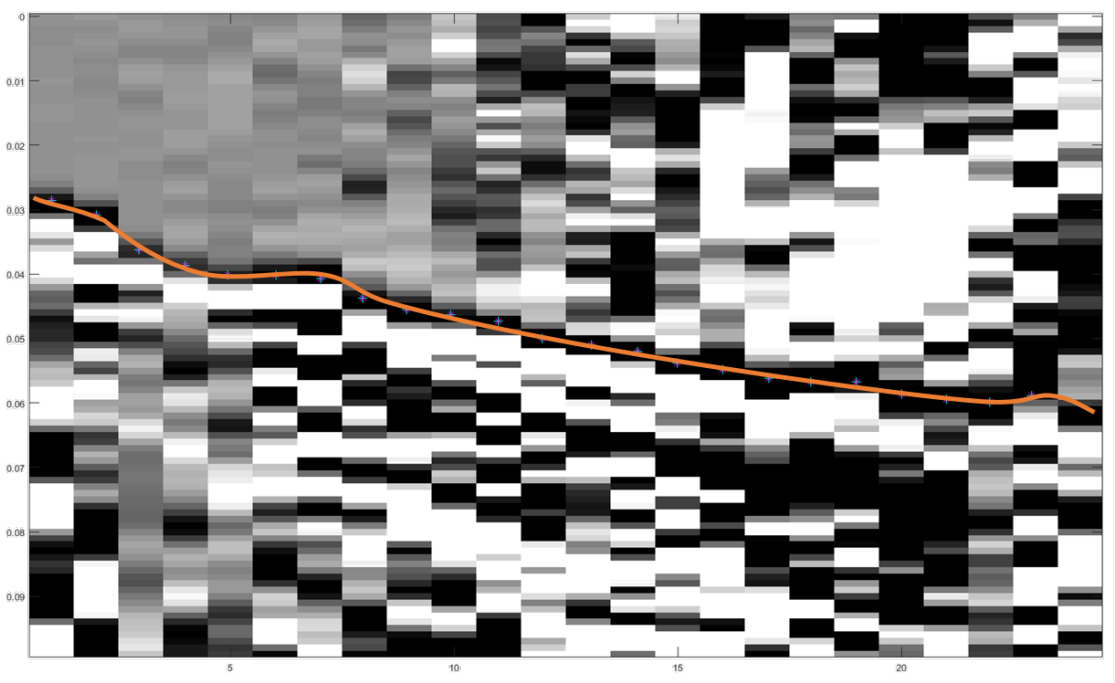

Figure 29: P-wave picking in vertical component for first source point

Once all the first arrivals have been picked on the seismograms, a final SEGY file is created. Such file is then loaded into Madagascar for further processing and seismic inversion. Madagascar runs in Linux OS. To work with the data, command lines are used.

Two models were generated with different inversion methods. The first method used is first arrival traveltime tomography, and the second method is full waveform inversion.

First arrival traveltime tomography (FATT) inversion is a robust tool for near-surface velocity estimation. This method produces high-resolution models. Inversion produces non-unique results, but full waveform inversion (FWI) is used to favor minimum structure solution which gives the highest probability among all non-unique solutions mathematically (Jiang and Zhang, 2017). The result of FATT inversion is shown in Figure 30.

FWI is a nonlinear iterative minimization process, which works by matching the waveform between the synthetic data and the seismogram, where the synthetic data is

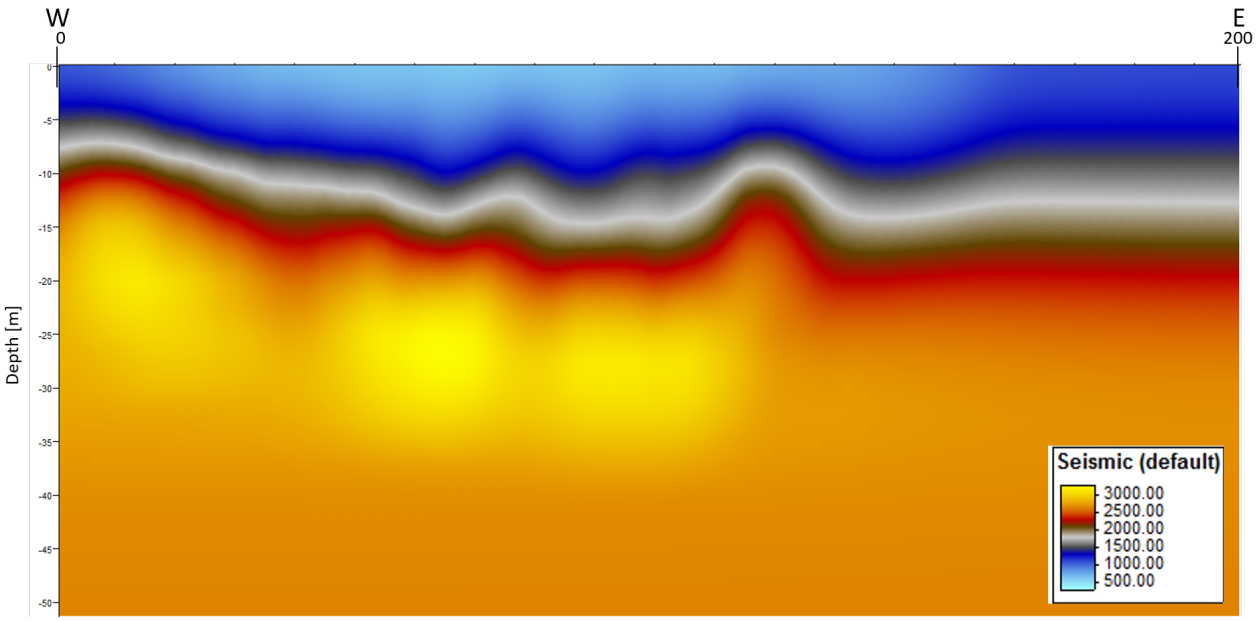

Figure 30: First arrival traveltime tomography inversion

obtained by a numerical solution of the wave equation. Full-waveform seismic inversion provides a general mechanism for reconstructing earth models from observed ground motion.(Burstedde and Ghattas, 2009). The capability of FWI to enhance 2D models has been demonstrated with blind tests, and comparing these results with the ones obtained using ray-theoretical method has a better correspondence. (Chen, 2011). Thus, this model was generated as an effort to have a more reliable inversion of the data. The obtained model is shown in Figure 31.

The drainage channel added noise in the horizontal component, which made it difficult to work with, or pick the first arrivals for the S-wave. Given that the line was located next to the active quarry, the environmental noise was also unavoidable. So the S-waves were not used for inversion.

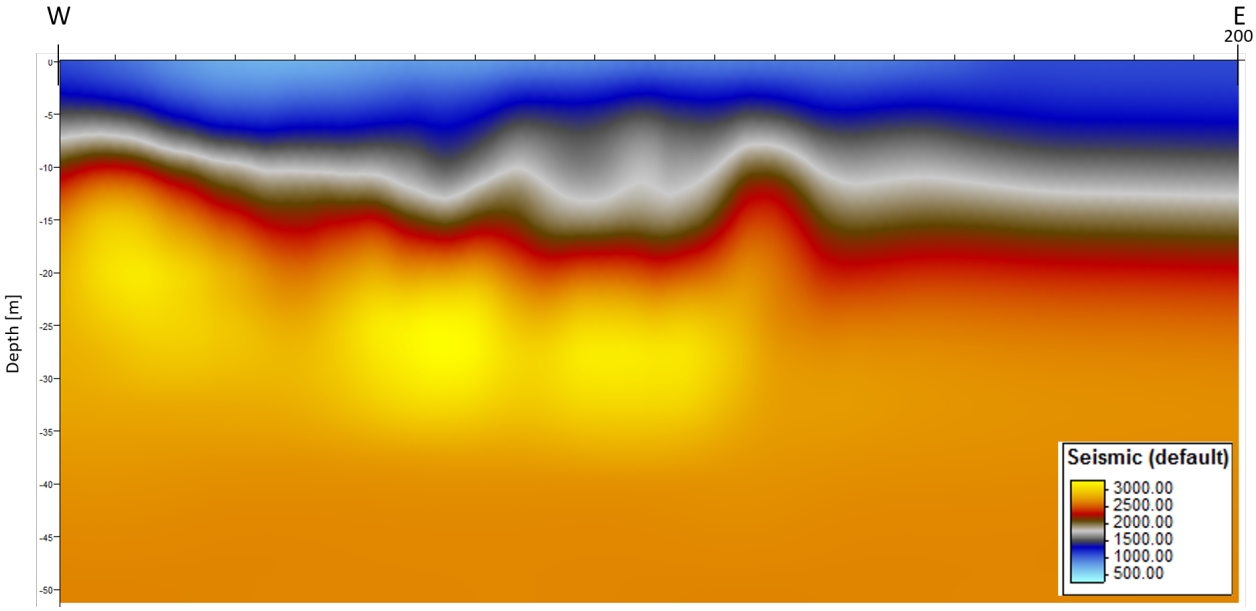

Figure 31: Full waveform inversion

8. Interpretation

8.1. GPR interpretation

The depth-converted lines were loaded in Petrel, and the main structures were interpreted. The scale is 1:1. The soil layer is too thin and it appears as a narrow line in the depth converted images. For practical reasons it will not be marked on the final interpretation. For clarity, the GPR interpretation will be divided in its correspondent areas.

8.1.1. Undheim GPR interpretation

In Figure 32(a), the basement is at a depth between 12 and 16 m from the surface. A big chaotic area in the sand is interpreted as moraine deposits/dead ice. The data obtained from hyperbolic matching shows an EM velocity of 12 cm/ns. Usually the moraine deposits are poorly sorted, with low compaction, and according to the literature, this type of deposits are inter-fingered in the massive sand body. The shape of the moraine deposits is similar to that of a lake. By comparing this line with the map view in Figure 26, it is possible to observe a dead ice feature at the southwest of the line, so this can be interpreted as dead ice. At the northernmost area of the line, near distance zero, it is possible to see the shape of onsets, most likely generated by the glacial flows in the area.

Figure 32(b) shows a higher basement near the slope where a moraine has been interpreted. The depth to the basement here is 7 m below the surface, but at the end of the line, the basement goes as deep as 20 m. The onsets are located in the same direction as in the previous line, which supports the theory of glacial flows. Two chaotic bodies are found in this line and they possess the same velocity as the moraine/dead ice from line 13.

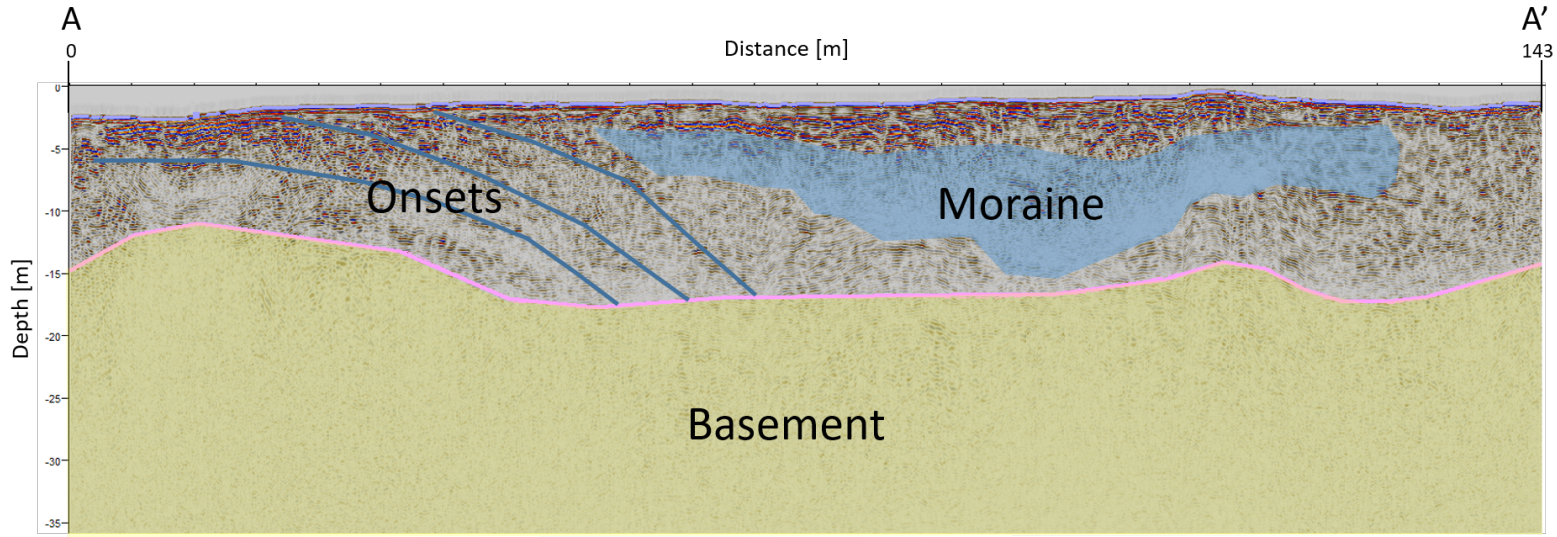

(a) GPR line 13 interpretation

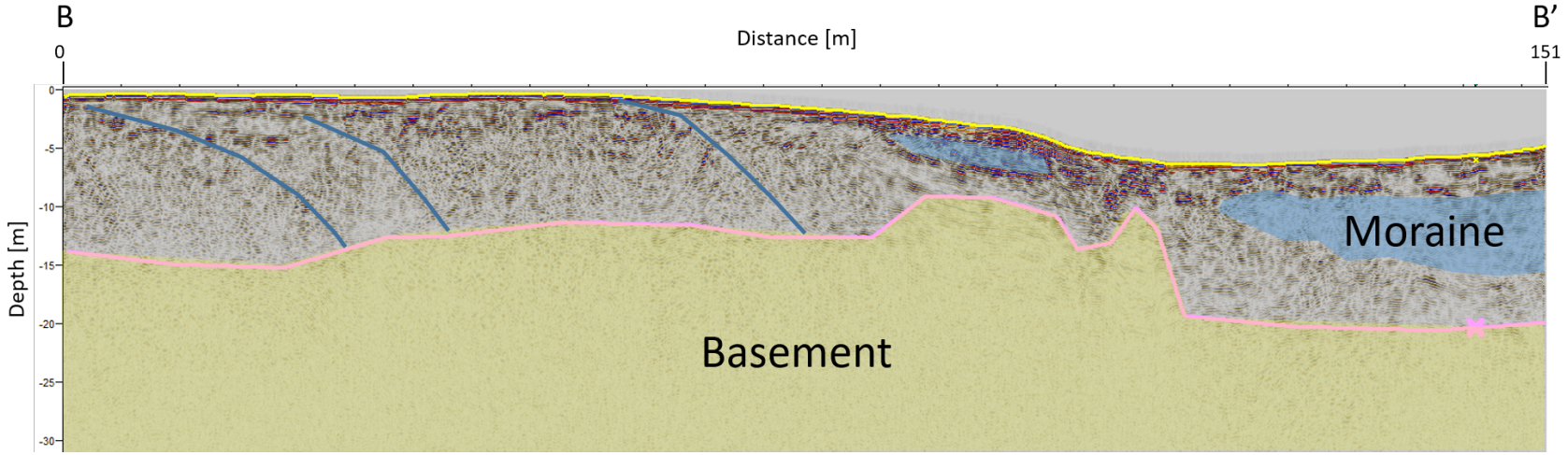

(b) GPR line 15 interpretation

Figure 32: GPR lines 13 and 15 interpretation

In Figure 33(a), three moraine bodies are identified at a depth no greater than 10 m. The onset features seen in the previous lines are present, and are terminated in the basement. The basement has a depth between 15 to 20 m.

On the other side, Figure 33(b) does not show the glacial flow features. By comparing the line with the location in the geological map from Figure 26, it is possible to see that the southernmost part of the line coincides with another dead ice feature, and again the interpreted body looks like a lake. A second moraine is interpreted at the end of the line with a bigger length than the previous interpretations. The basement is at a regular distance from the surface, located at 10 m under the surface.

One important thing to notice in this Figure is that the data is consistent. By placing both lines in their 3D spatial location, the interpreted moraine coincides in depth, as well as the depth of the basement.

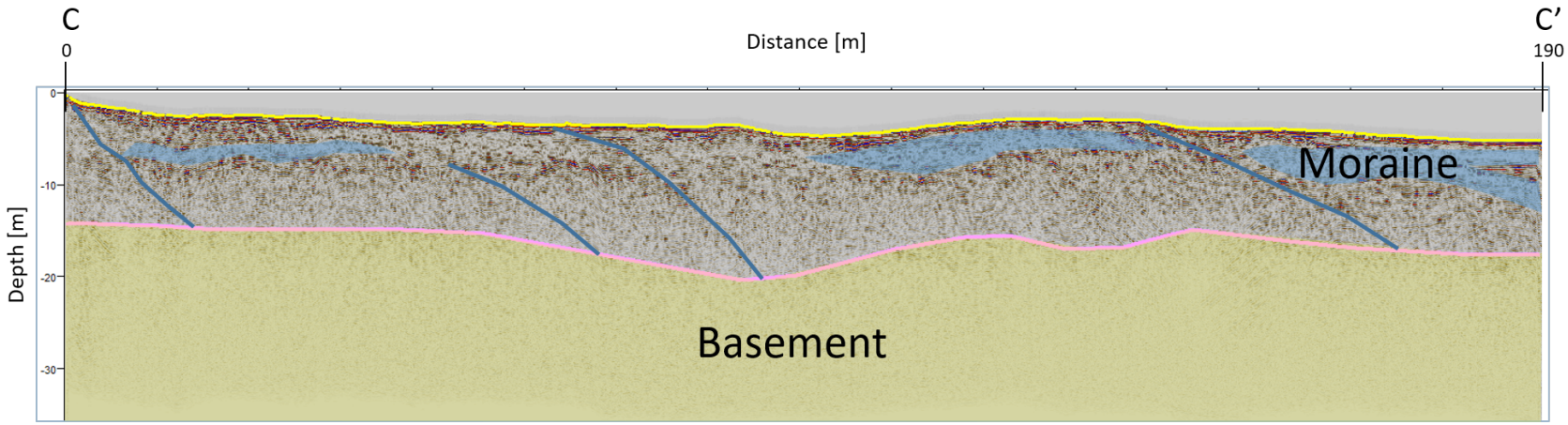

(a) GPR line 16 interpretation

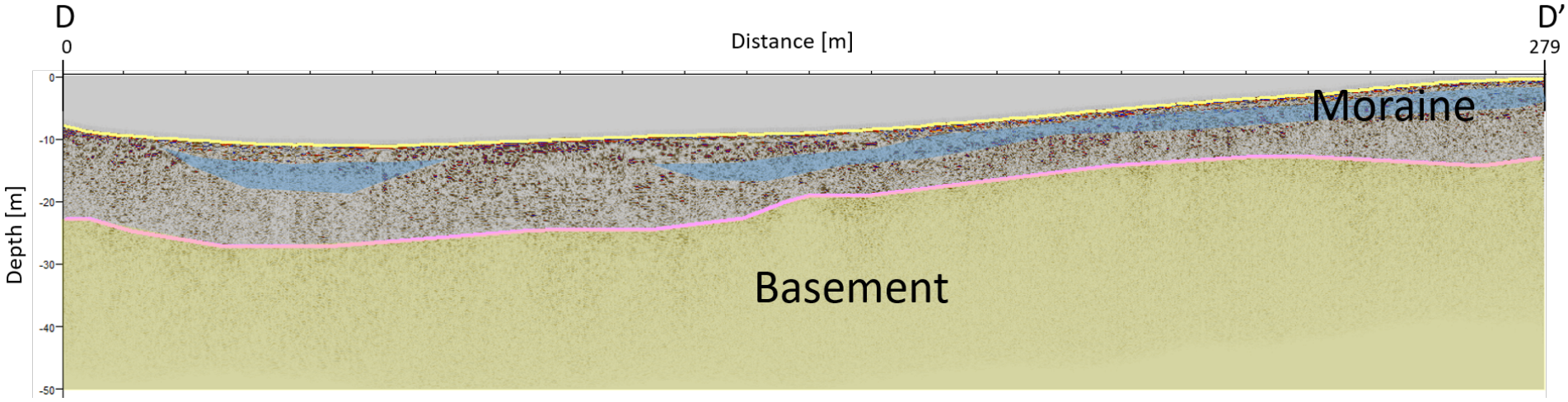

(b) GPR line 17 interpretation

Figure 33: GPR lines 16 and 17 interpretation

Figure 34(a) shows a moraine in most of the extension of the line, with one feature of the glacial flow. The basement is at around 15 m depth across all the line.

GPR line 19 is shown in Figure 34(b). This line is parallel to line 18, and as such, the same feature on a moraine, which covers most of the line is present. Two features interpreted as onsets are seen in this line, and these are marked with blue lines showing the direction of the glacial flows. The topography of this line is not accurate. This could be due to some noise during the acquisition, since the topographical information comes from the GPS inside the GPR equipment. However even with the low accuracy of the topography, it is possible to observe continuity of the moraine across the other GPR lines.

As with the previous image, placing the lines in a 3D setting shows the data is consistent between lines and the basement, and moraine bodies described seem to match their counterparts in intersecting lines.

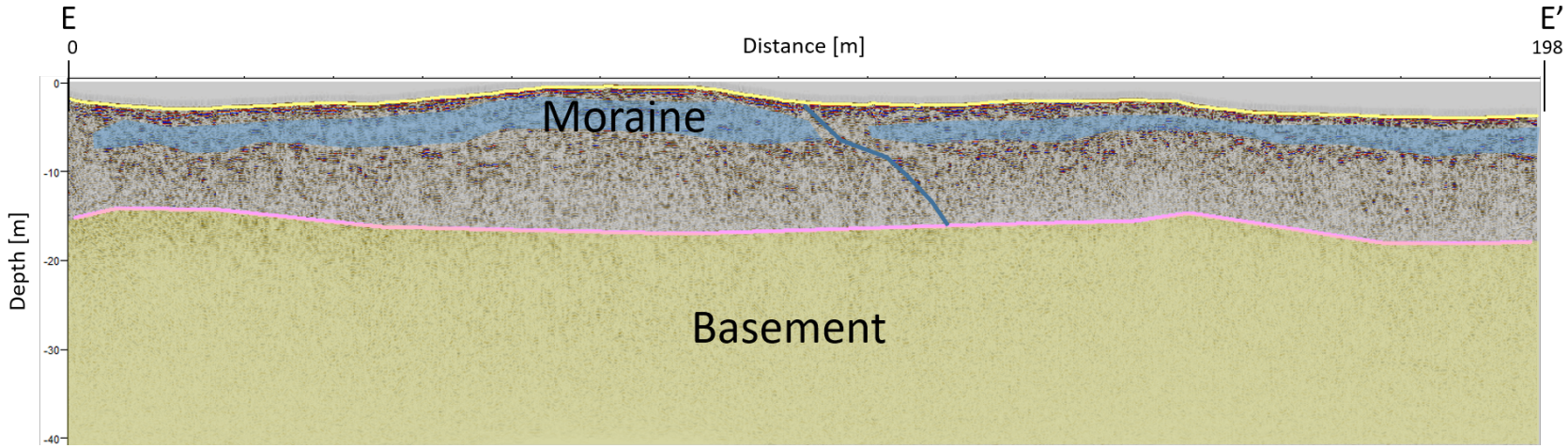

(a) GPR line 18 interpretation

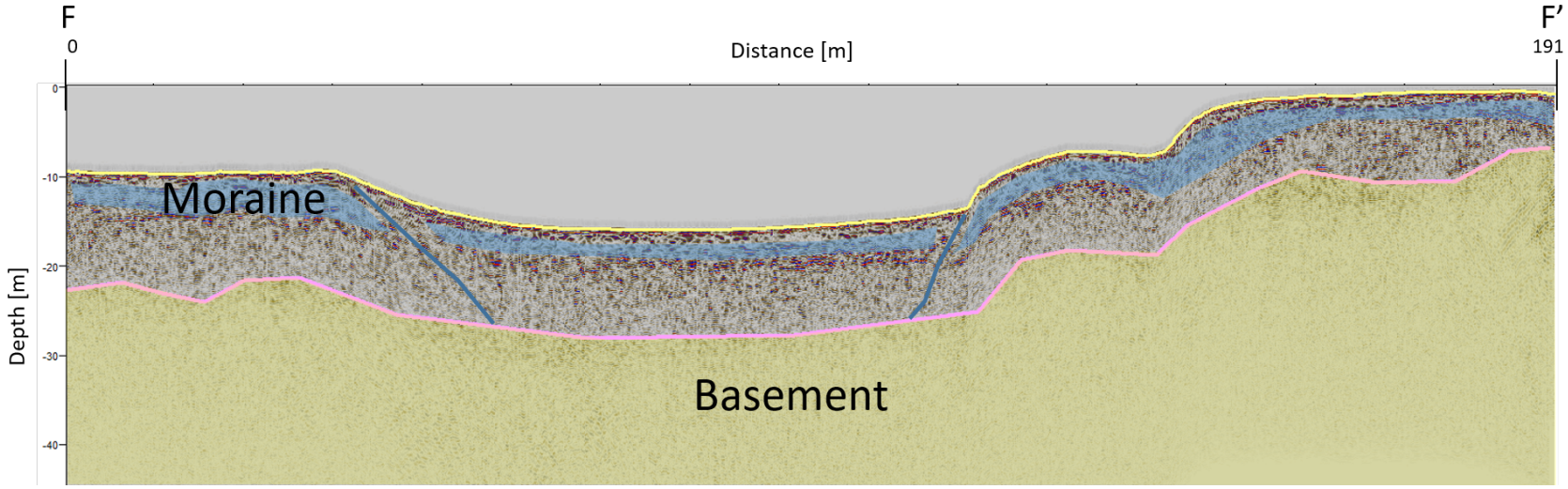

(b) GPR line 19 interpretation

Figure 34: GPR lines 18 and 19 interpretation

GPR line 20 is shown in Figure 35. This line was acquired on the highest area accessible in the quarry. Since this line is topographically higher than the rest, it is expected to see the basement at a deeper location, in this case up to 30 m deep. A chaotic area interpreted as a moraine is also found here. At the end of the line is possible to see the influence of the rough terrain in the quality of the data. Some traces were skipped creating a gap in the data, which could not be fixed with spatial interpolation.

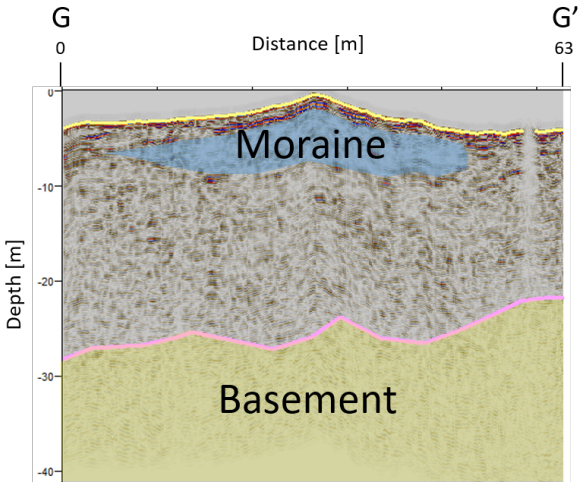

Figure 35: GPR line 20 interpretation

GPR lines 21 and 22 were acquired in the same position but in different directions. This was made with the goal of reviewing how consistent the data is, and make sure the repeatability was present. The same procedure was done with lines 23 and 24. In the general depth converted model, it is possible to see this mirror effect in both lines; in Figure 36 it is easier to observe.

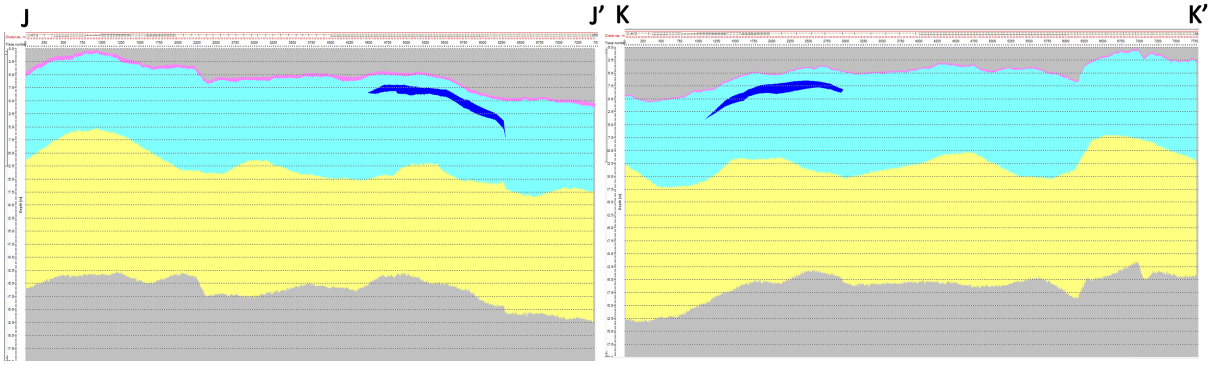

Figure 36: GPR consistent data in line 23 (left) and 24 (right)

Given the fact that the data is consistent, only one line will be used for the interpretation.

Figure 37(a) shows line 21. This line is important since it is parallel to the cross-section seen in Figure 4. In this line, a moraine body is interpreted and, following the proposed geometry of a moraine going under the surface, the interpretation would confirm this idea. The basement is marked between 18 and 20 m under the surface, and two onsets are marked in the line.

Figure 37(b) shows line 23, the longest acquired line that is closer to the mountain. According to the geological map near this area, it is possible to encounter moraine deposits and bare mountain. The mountain corresponds to the basement, which was uplifted. This can be verified by the shallow basement along the line. The moraine deposits cover a big part of the shallow area, and the glacial flow features are marked in the line.

The interpretation of the basement for all the GPR lines was performed in Petrel, and using a gridding algorithm, a depth surface for the basement was generated. This can be seen in Figure 38.

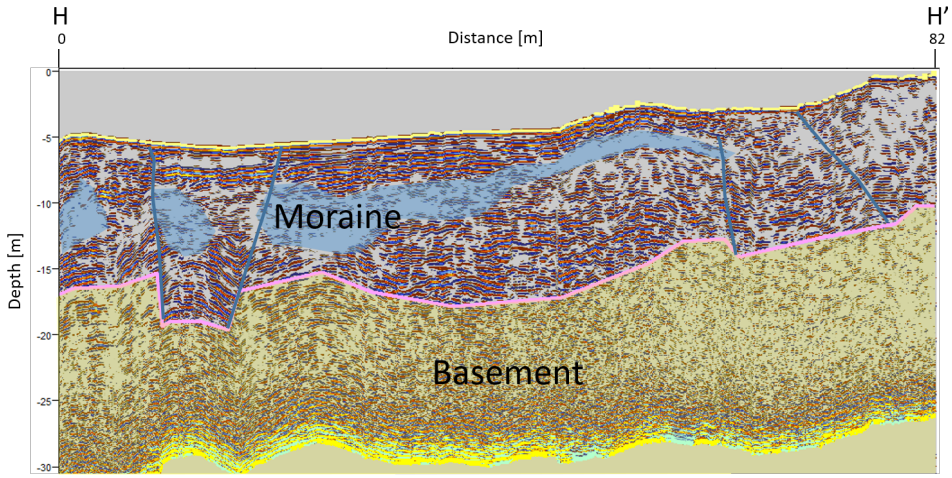

(a) GPR line 21 interpretation

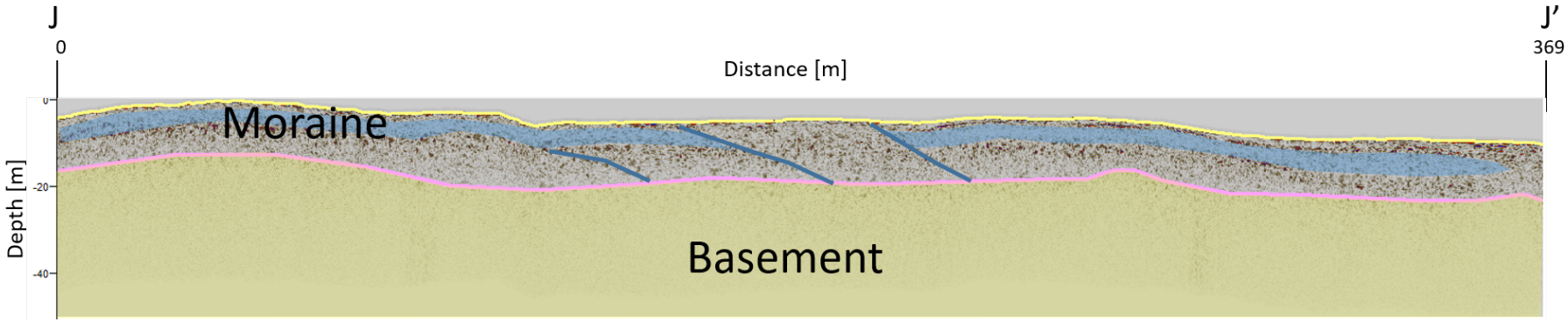

(b) GPR line 23 interpretation

Figure 37: GPR lines 21 and 23 interpretation

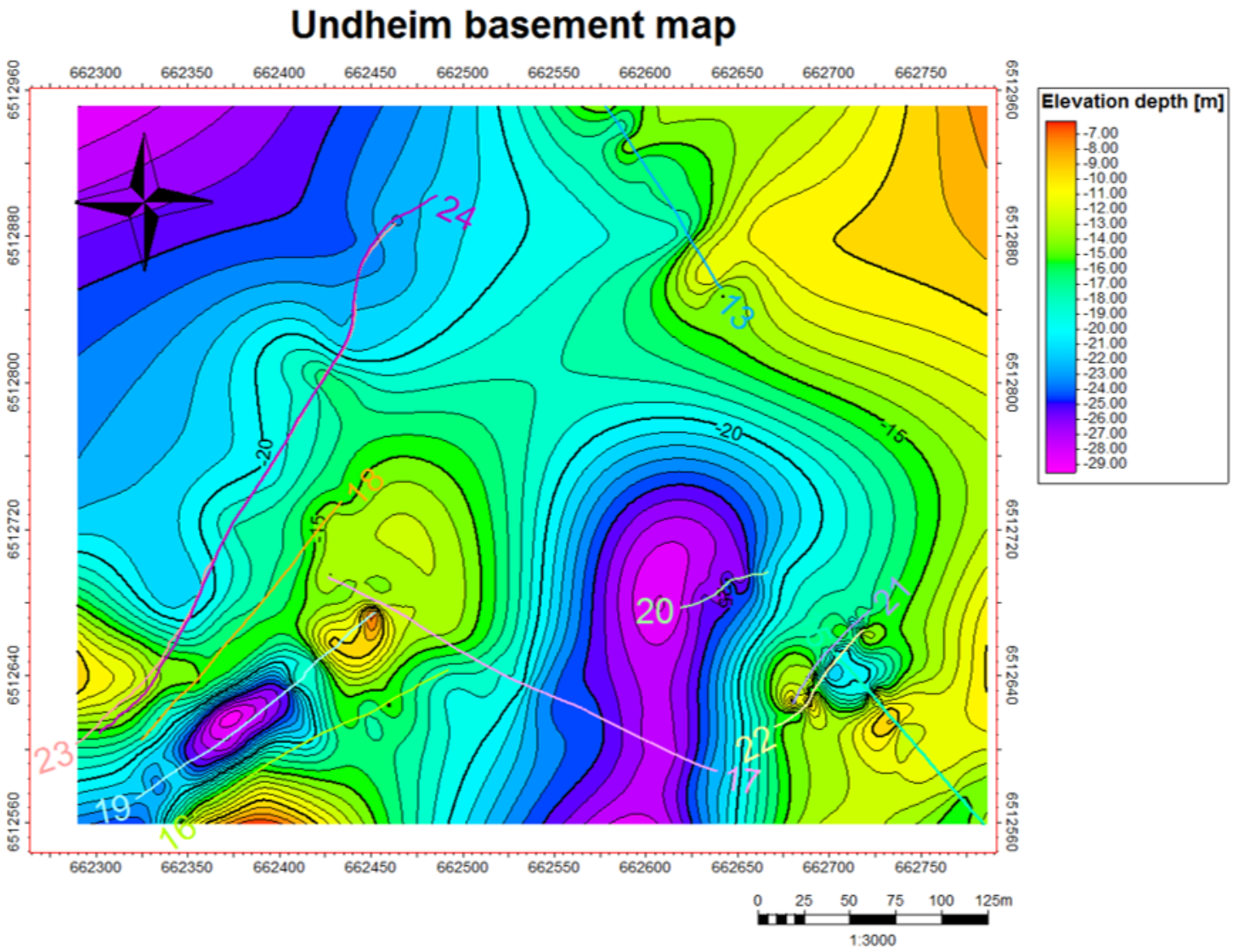

Figure 38: Basement depth map in Undheim

8.1.2. Bryne GPR interpretation

In the Bryne site, as seen in Figure 27 swamp deposits are present. These can be seen in three of the four acquired lines. As with the previous site, metamorphic basement is present. Lines 8 and 9 were acquired in the same location, and as with the previous location, only one of the lines will be shown here to avoid redundancy.

Figure 39(a) shows GPR line 9. This area is mainly composed of clay, which has a low velocity. This will make the results shallower, and the quality of the data beyond 30 m is not reliable, but this is not an issue since it is possible to interpret the basement with the aid of seismic attributes as discussed in chapter 7. The metamorphic basement is shallow, with depths ranging from seven to 15 m below the surface. There are no major structures seen in this line.

GPR line 10 is shown in Figure 39(b). In this line, it is possible to see a chaotic body in the middle of the line marked in red. Comparing the line with the geological map this feature coincides with the swamp deposits, so it is interpreted as such; it presents a velocity of 5 cm/ns. A low velocity can also represent a higher water saturation, which agrees with the theory of swamp deposits in the area. The basement is at approximately 15 m below the surface.

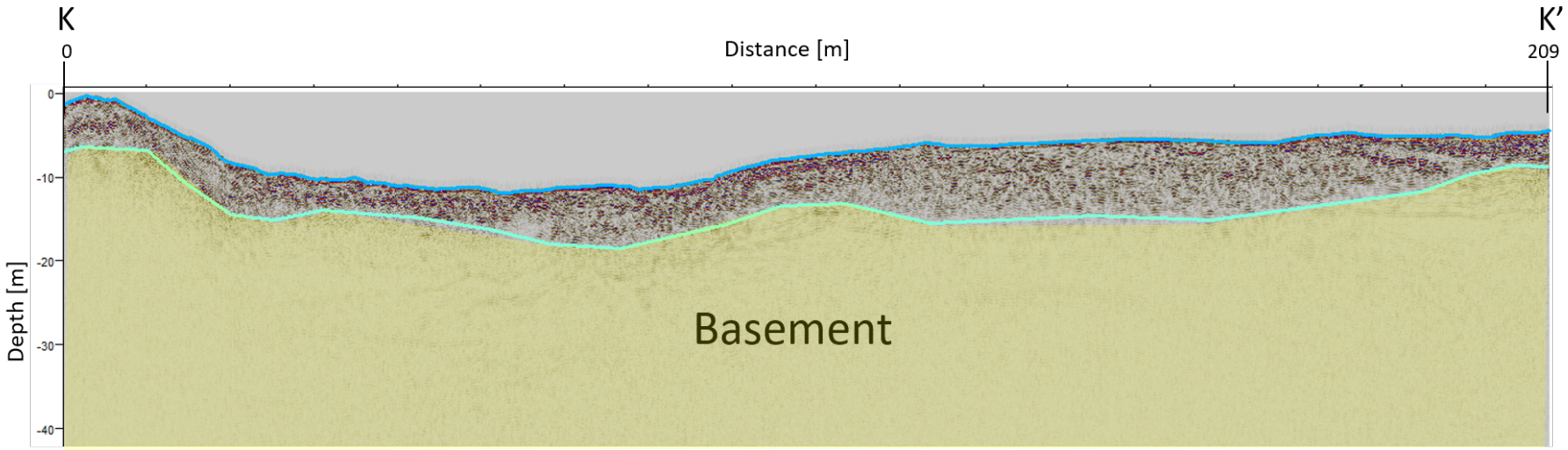

(a) GPR line 9 interpretation

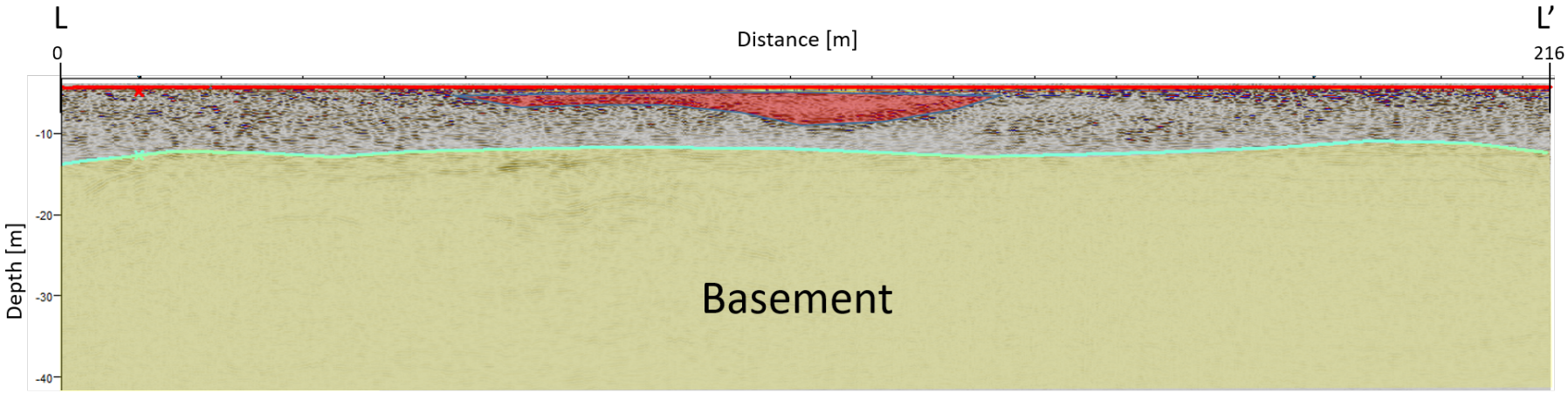

(b) GPR line 10 interpretation

Figure 39: GPR lines 9 and 10 interpretation

GPR lines 11 and 12 are also over the swamp deposits, so it is expected to see the same features and velocities as seen in Figure 39(b). The data coherency has been proven, so it is expected to find the basement and swamp deposits at the same depth throughout the lines.

GPR line 11 is shown in Figure 40(a). The swamp deposits are in the northernmost part of the line, and the deposits are seen as chaotic bodies with low velocity. The metamorphic basement is seen at a shallow depth, no more than 10 m deep.

In Figure 40(b), line 12 can be seen. As observed in Figure 27 this line is located on top of the swamp deposits, and as such, these deposits can be seen along the whole line at a shallow depth. The basement is located at around 15 m below the surface.

A basement depth map was generated with the interpretation of the lines in Bryne. The locations of the acquired lines are marked for reference. The gridding algorithm used was convergent interpolation, since the density of the data is low. The depth of the basement is more accurate near the lines, but the approximation from the grid should be quite close to reality. The depth map is shown in Figure 41.

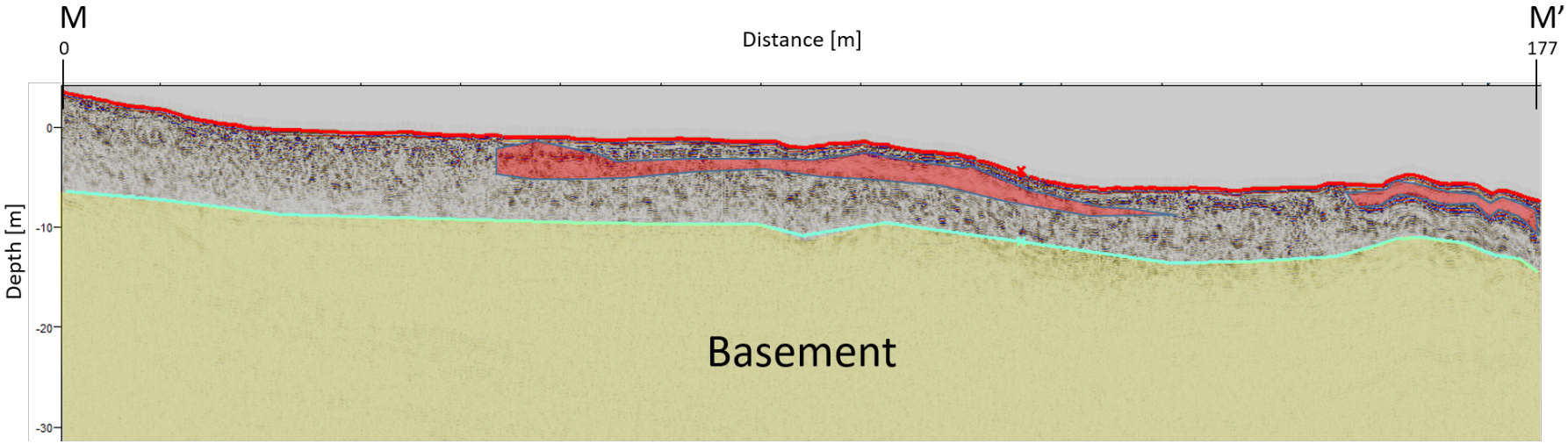

(a) GPR line 11 interpretation

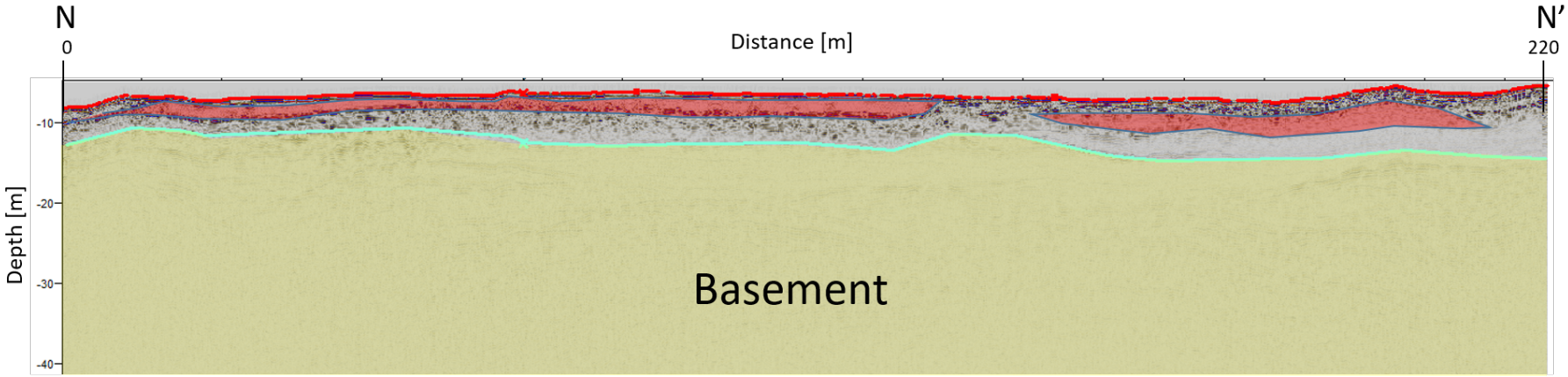

(b) GPR line 12 interpretation

Figure 40: GPR lines 11 and 12 interpretation

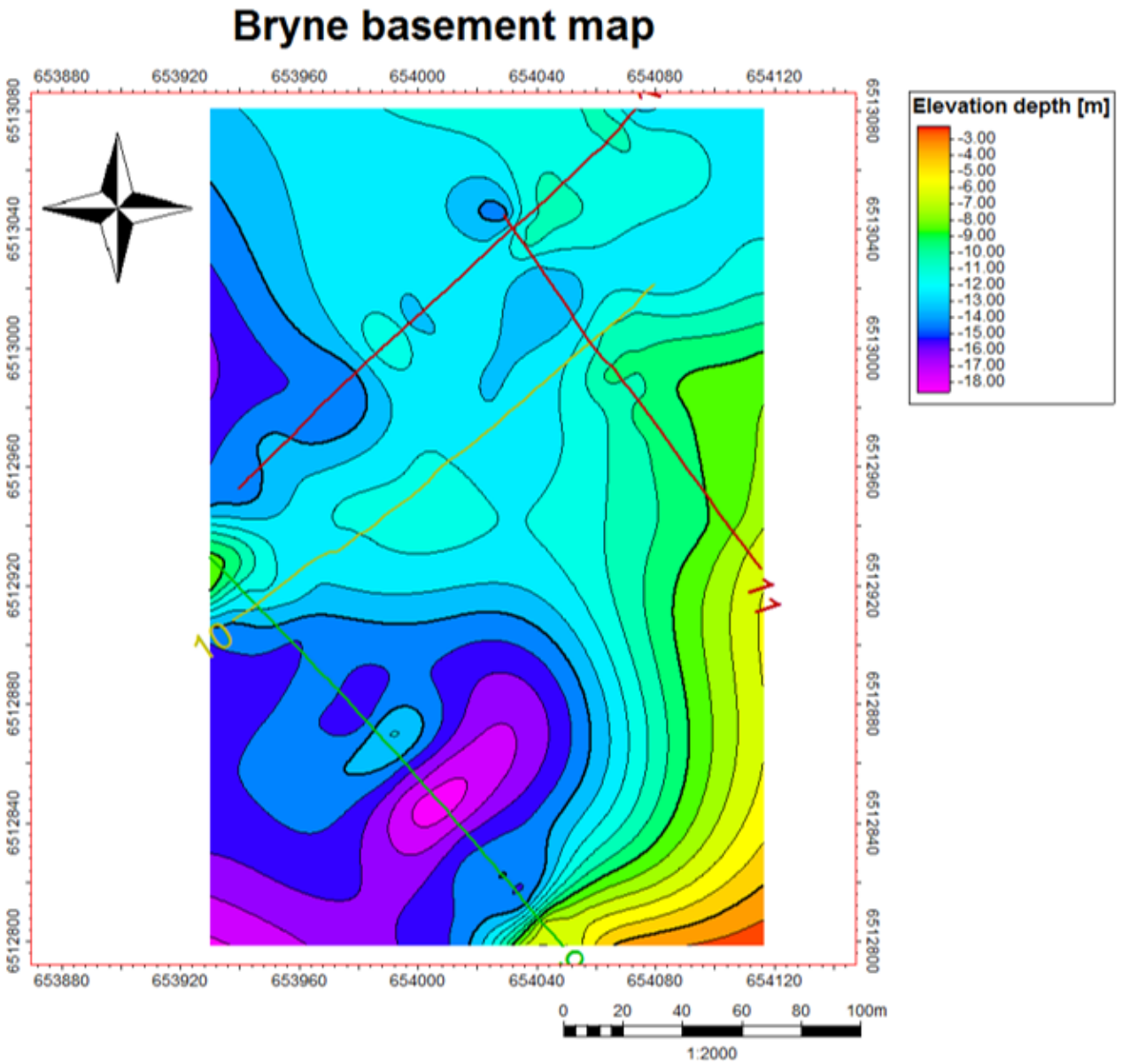

Figure 41: Basement depth map in Bryne

8.1.3. Sandnes GPR interpretation

On the last site, Sandnes, the geological map shows only moraine deposits. As well as in Undheim site, it is possible to see structures reminiscing glacial flows, looking as onsets. A thin layer of soil is present in all the lines, the majority of the material under the soil is interpreted as moraine material, but chaotic structures with high velocity are seen under each onset. Given the glacial nature of the area, these deposits could be formed of till, which is the general term for deposits directly deposited by ice (Nichols, 2009), and given the location of these, under the assumed structures of glacial flows, it would fit the theory.

An undefined lithology found under the moraine deposits falls into the shale velocity by comparing with the table 1. Another possibility could be debris material, which is composed of different sediments, boulders and pebbles of different lithologies, etc., so it would be difficult to have a definite value for it, and this cannot be confirmed just with GPR data. In the following interpretation, those materials will be referred to as high velocity deposits and undefined lithology.

Line 25 in Figure 42(a) shows onsets, which have been related to glacial flows inside the moraine deposits. Between each of these flows, a high velocity body is found. This could be the material dragged by the moraine during the glacial flow. A layer of undefined material is found under the moraine deposits. The metamorphic basement is found in depths between 25 and 35 m.

Figure 42(b) shows line 26. This line is perpendicular to line 25 and the depth of the basement, and undefined material is consistent with those of previous lines. Another body of high velocity is found. This has the same velocity as the material found in line 25. The basement appears shallower near the end of the line; however, in this area there is a small hill, so this geological high could be related to the shallow basement.

Line 27 is shown in Figure 43(a). The layers defined in the general model are also present here; the high velocity deposits are present in the hill area. The undefined lithology layer is present in this line under the moraine deposits. The metamorphic basement is at around 30 m.

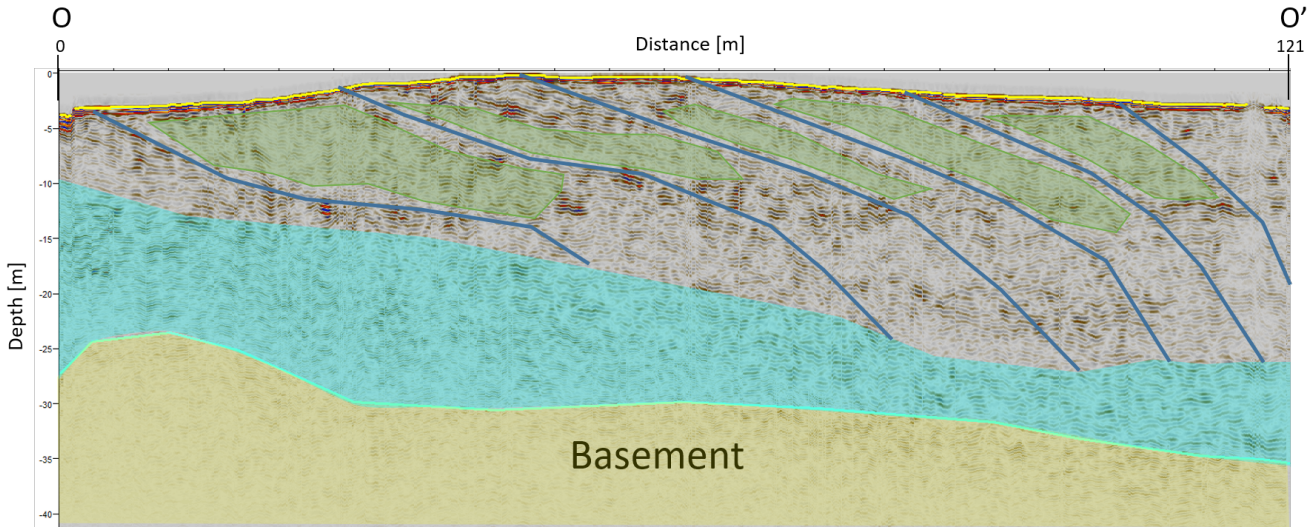

(a) GPR line 25 interpretation

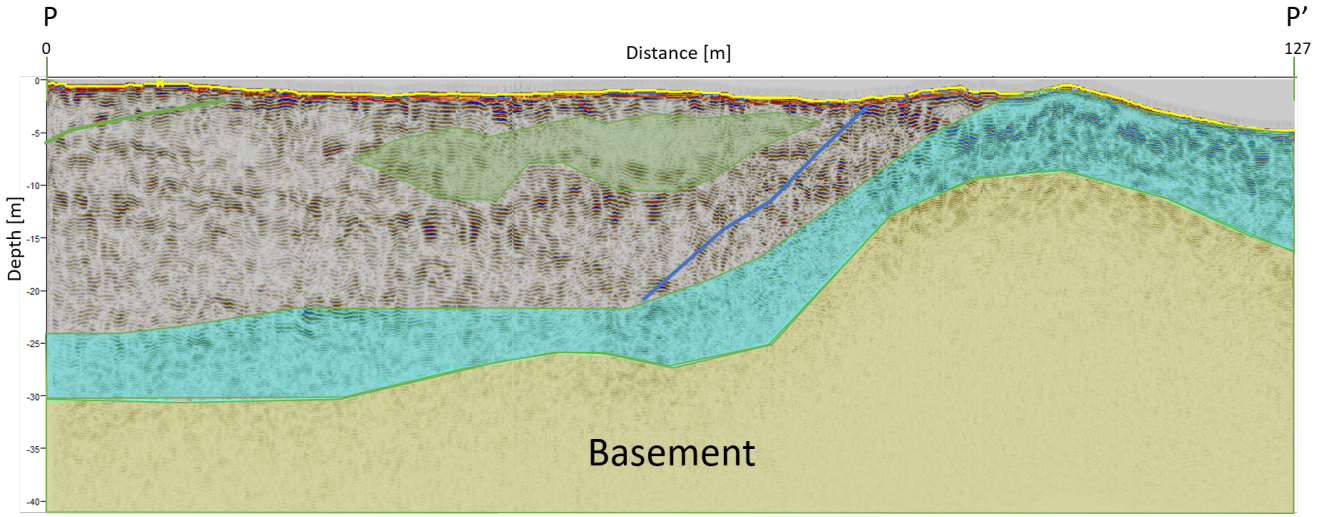

(b) GPR line 26 interpretation

Figure 42: GPR lines 25 and 26 interpretation

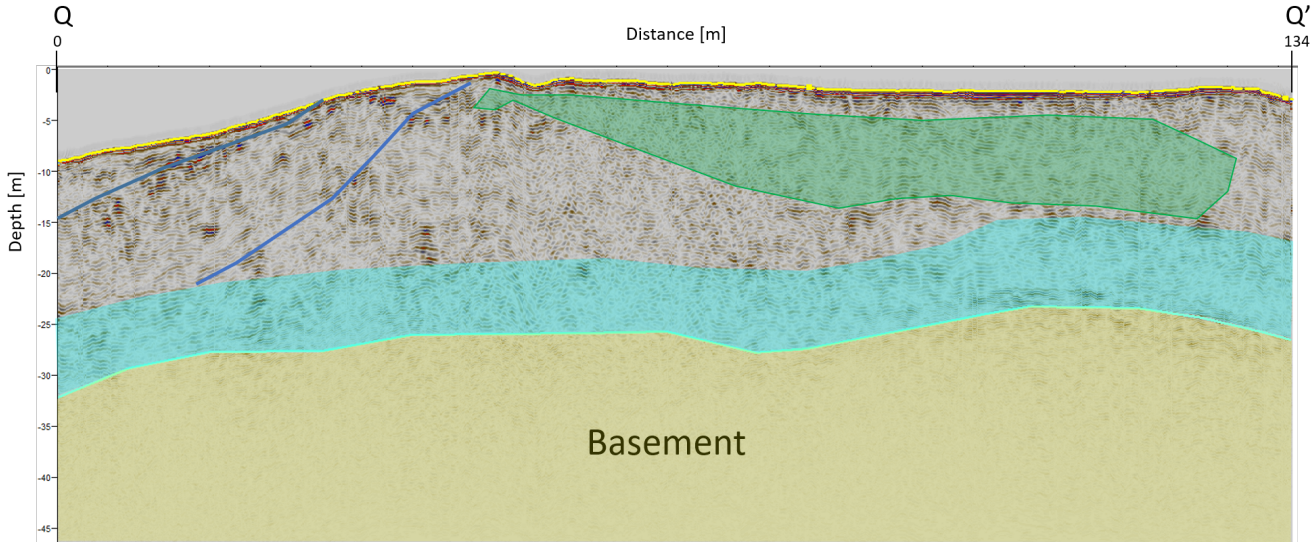

(a) GPR line 27 interpretation

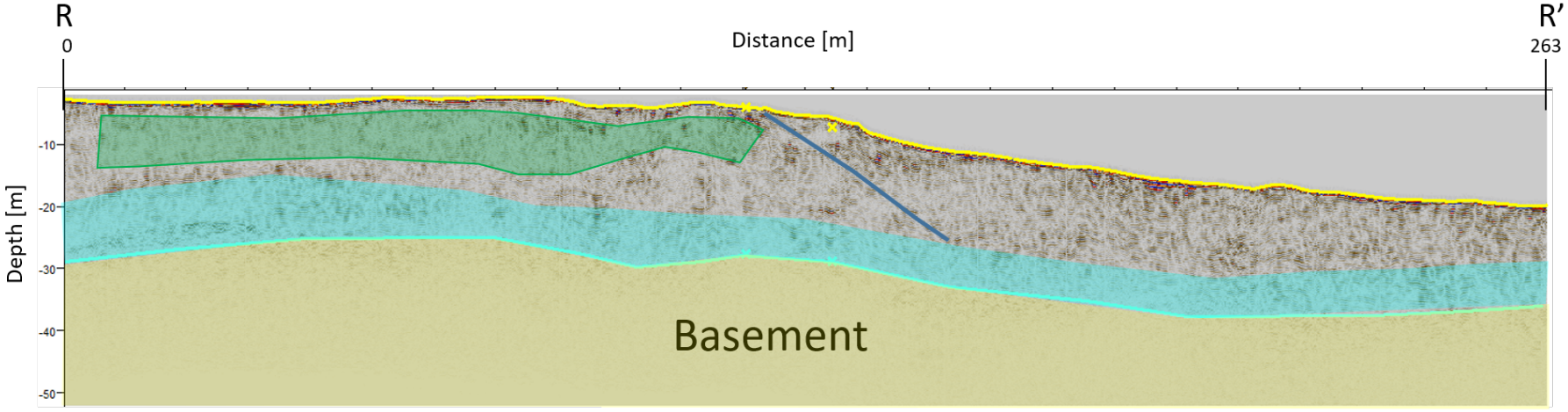

(b) GPR line 28 interpretation

Figure 43: GPR lines 27 and 28 interpretation

Line 28 was acquired from the end of line 27 but further down the hill. In Figure 43(b), the beginning of the line is a mirrored image of line 27 because of its location. Further down the hill there are no more high velocity deposits. The depth of the basement is consistent in both lines

Line 30 is seen in Figure 44. This line is the shortest. The structures, which are related to glacial flows are seen in here, and the basement is at depths between 20 to 25 m.

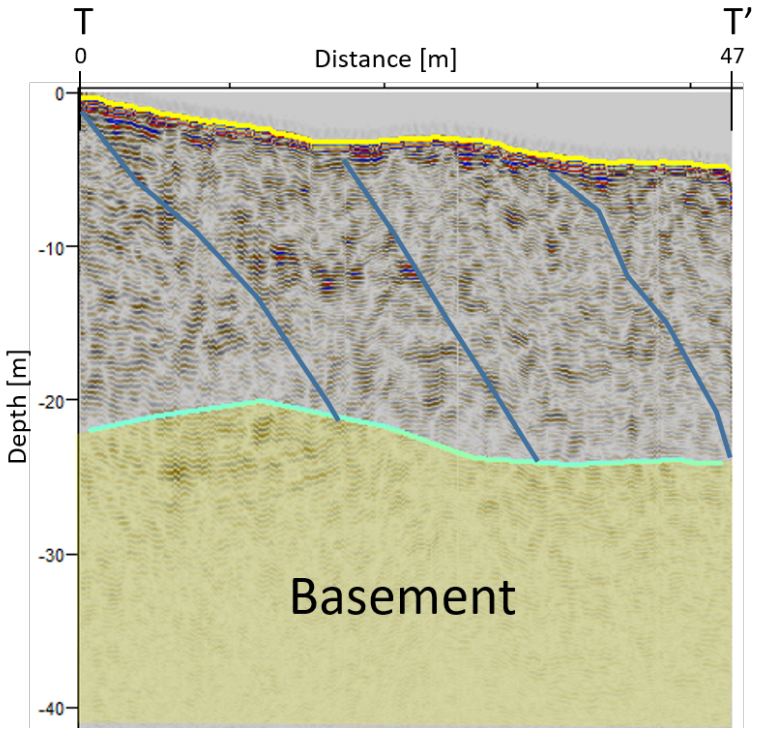

Figure 44: GPR line 30 interpretation

Figure 45 (a) shows GPR line 29. This line does not show the layer of undefined material, but the basement depth is consistent with the interpretation of the intersecting lines. One body of high velocity deposits is identified as well as one of the onsets related to glacial flows. In Figure 45 (b) line 31 is interpreted. This line is parallel to line 25, so similar structures are expected to be seen. In this line the glacial flows are seen with the bodies of high velocity between each one of them. The basement is seen between 25 and 30 m below the surface.

As with the previous two sites, the interpretation of the basement was transferred to Petrel and a basement map was created. Figure 46 shows such map.

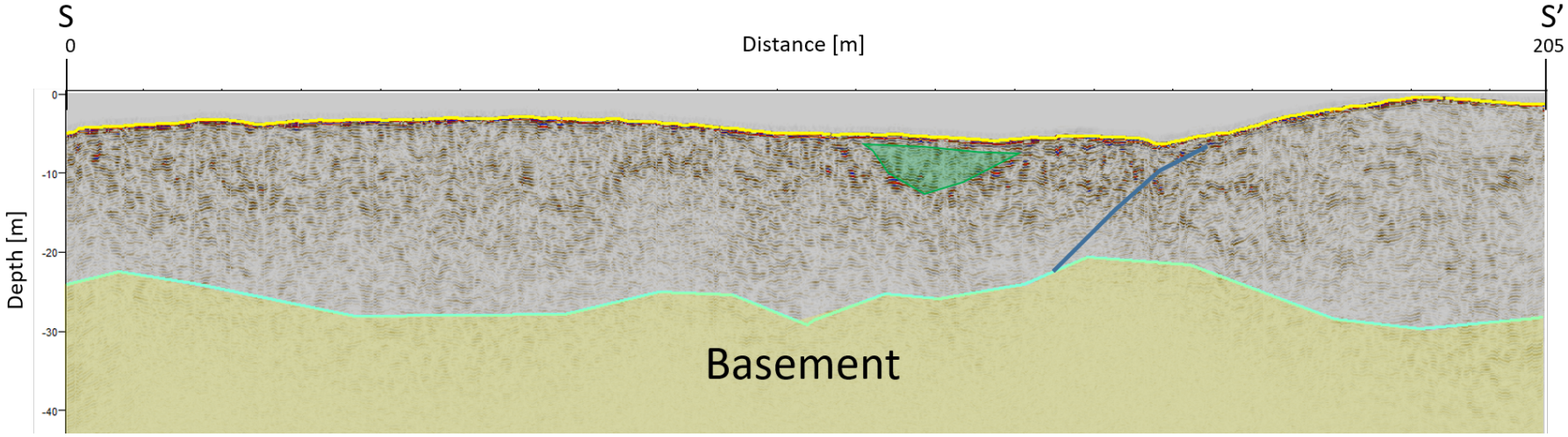

(a) GPR line 29 interpretation

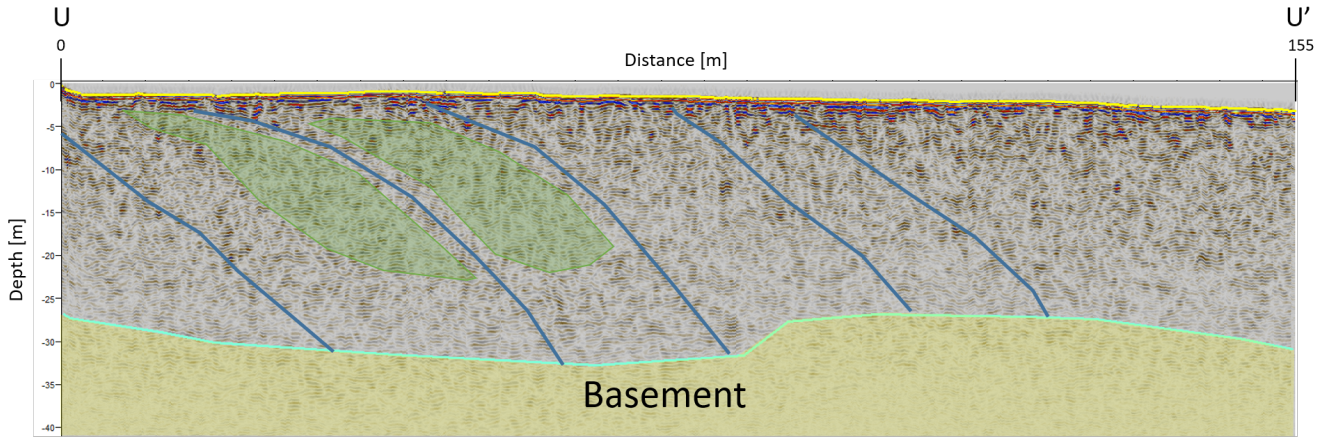

(b) GPR line 31 interpretation

Figure 45: GPR lines 29 and 31 interpretation

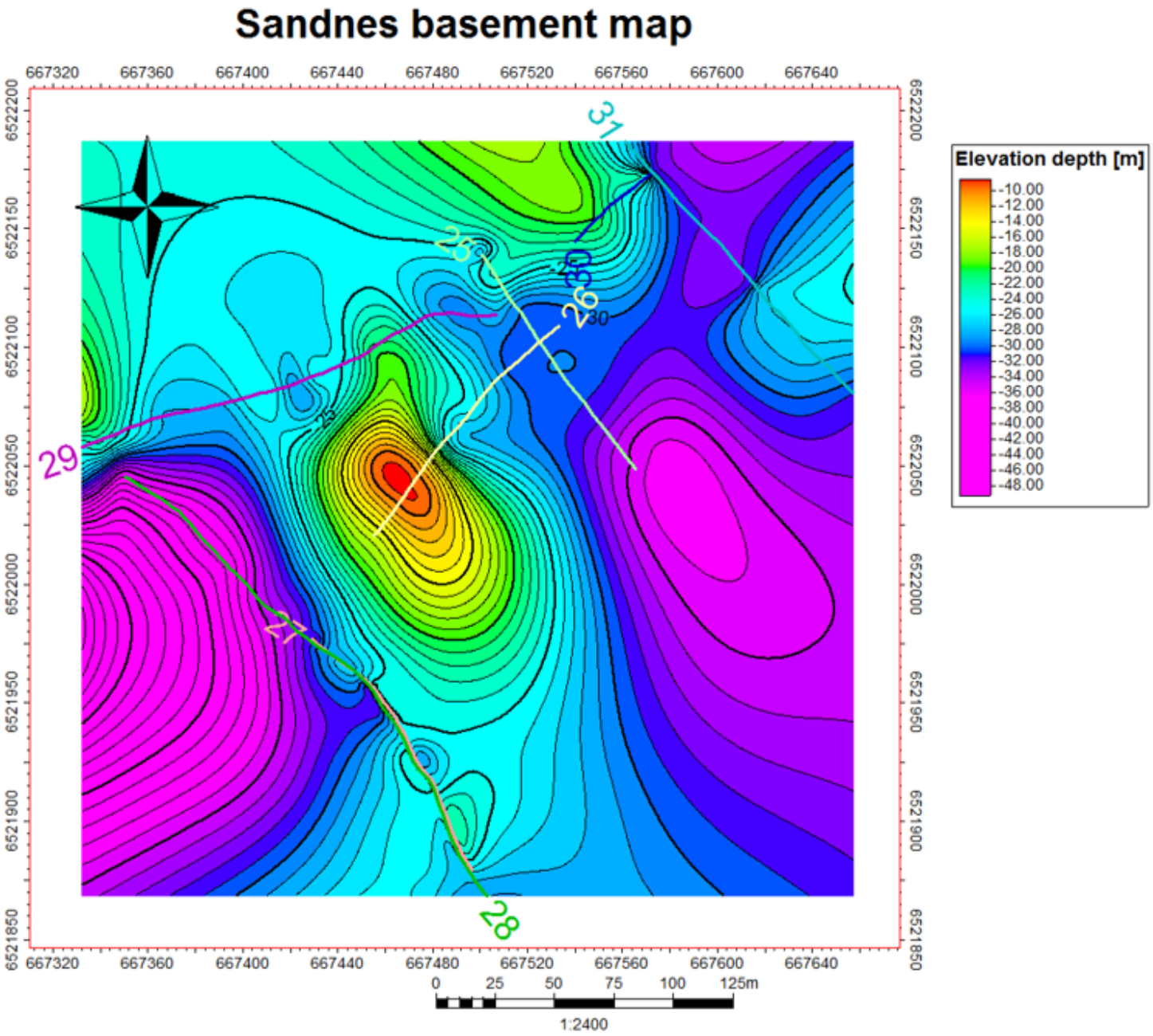

Figure 46: Basement depth map in Sandnes

8.2. Seismic interpretation

8.2.1. Undheim seismic interpretation

The models created in Madagascar with P-waves are FATT and FWI as seen in Figure 47. Both models are in the same range of values. The obtained geometries in the inversions are similar, which shows that both methods are good at avoiding the non-uniqueness of the result by displaying consistent results. In FATT, the velocities near the surface are lower than those obtained in the FWI. The basement is seen in both models at the same depth and with the same velocities, so this will be a good marker for the comparison with the GPR data.

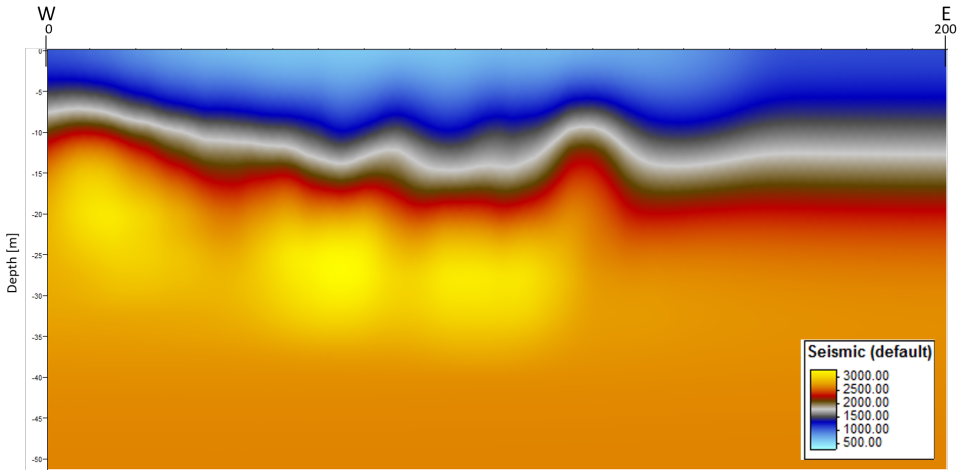

(a) VP FATT

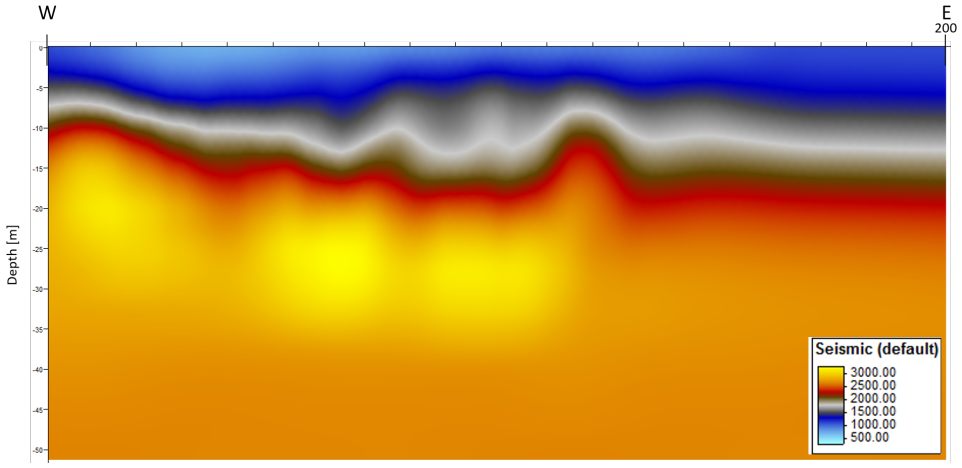

(b) VP FWI

Figure 47: Seismic inversion, (a) FATT (b) FWI

8.3. Combined interpretation

The acquired seismic is longer than the GPR line, so it was necessary to crop the seismic inversion to the right location where it overlapped the GPR data. By doing this, it is possible to see the location of the basement is mostly identical in both methods, which would work as a quality control measure to determine the validity of the velocity model created with the radar data.

By overlapping both results, it is possible to see the GPR data has better lateral resolution. This is due to the closely spaced traces of the data. The body, which was identified as dead ice/moraine in the GPR line is not seen in the seismic line; however, a low velocity layer is identified in the seismic at the same location.

The structures interpreted as onsets, are not seen in the seismic, but if the boundary between the low velocities is marked then it seems to match the onset marked on the south of the line (near point A). This would complement the theory of glacial flows in the area.

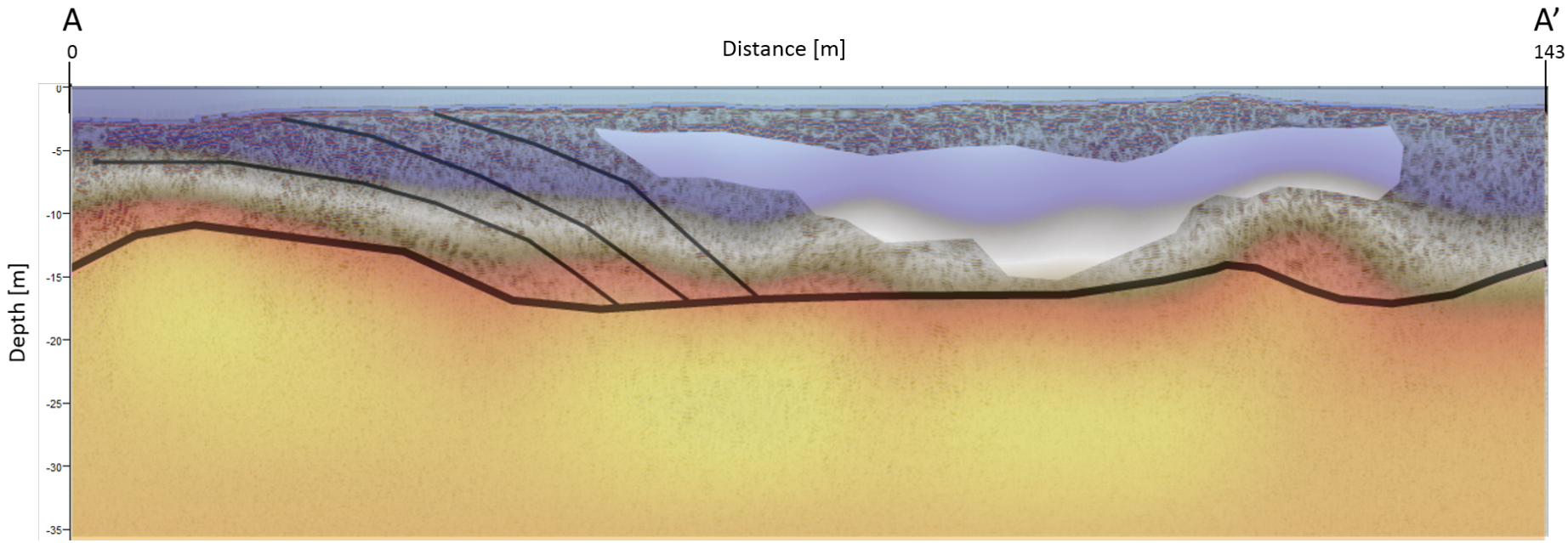

Figure 48: Combined GPR and seismic data in line 13, Undheim

9. Discussion

The glacier deposits are accurately mapped with GPR data. The main objective of this thesis was to create a combined model of seismic and GPR, however, not enough seismic data was acquired to make a proper comparison of the results, or to create a more advanced mapping workflow. The weather constraints were not taken into account in the planning of the acquisition. Furthermore, the first quarter of 2018 was extremely cold with average temperatures between zero and 7 °C (Norwegian Meteorological Institute, 2018), and without the proper tools for digging on frozen ground the seismic acquisition was postponed. Nonetheless, a proper tool for digging is now owned by the University of Stavanger, so in further seismic studies it would be recommended to perform the acquisition under cold climate. The frozen ground could help enhance the seismic waves and the data could be of better quality.

The processing used in the radar data provided good results. The limiting factor in this workflow is that it is only possible to use one velocity for the migration. In reality, the subsurface is composed of different materials. To have an even more accurate model it would be necessary to have the ability of using different migration velocities. This would create sections with better resolution. This could be done with a processing software different than the one provided with the acquisition equipment.

If the density of the GPR lines is increased, a geomodel could be constructed to see how the sediments are distributed in a 3D setting. With the current data it would be possible, but the lines are so sparse that the interpolation in between would not be accurate, making the results unreliable.

In a broader comparison of both methods, it is important to review advantages and disadvantages of each one. Some of the advantages of GPR are that is a non-destructive method (this characteristic makes it more appealing for landowners who refuse to have their land dug). It has no weather restrictions. Requires a short acquisition time, only one person is needed to perform all the work. The equipment is not big, so it can fit in a regular car. The disadvantage of this method is that in certain geological conditions with high conductivity, the EM will not penetrate deep enough and the scattering of the

waves will degrade the depth of penetration.

On the other side, seismic acquisition has several restrictions. It is an invasive method. It is dependent on a quiet environment, which is difficult to achieve near a city; this will require more processing to remove unwanted noise. The equipment is bulky and cannot be transported in regular car. Deploying the geophones can be time consuming and to speed up the process more than one person is needed. This is also true for the person acting as the source (with the sledgehammer) and one person recording data in the console. However, the advantage of seismic is that it is possible to penetrate up to several tens of meters even with a small source, and the conductivity of the materials in the subsurface is not an issue for the acquisition, however the stiffness and saturation are. Seismic exploration is a well-developed method, and it is possible to find more literature about processing workflows, and inversion methods.

Seismic acquisition combined with GPR data can provide reliable results. However, given the restrictions for the seismic acquisition, using a ground penetrating radar can be a good solution if high-density data is required in a short amount of time.

10. Conclusions

The Quaternary sediments of the Jæren area in Norway are constituted by glacial deposits, which have been subjected to erosion and uplift changing dramatically the geometry. That is the reason why it was necessary to perform this study, to map the glacial deposits.

Two near-surface geophysical methods were used: GPR acquisition, which works with EM waves to probe dielectric properties of the subsurface, and seismic acquisition data works with reflected and refracted waves generated by a source.

The data was acquired in three locations with different geology, the first one in the Undheim area next to an active sand quarry, the second in Bryne in a farming field, and the third in Sandnes next to a new quarry. All the sites had different lithologies, which made it easy to see the responses of the methods in different scenarios.

In Undheim, a cross-section was exposed, and it was possible to define the composition, which aided in the interpretation of the moraine deposits. Bryne is over clay area with swamp deposits, this was the most challenging area for the GPR since this type of material has high conductivity. In Sandnes most of the material was formed of moraine deposits, tills, and glacial sediments.

In total 23 GPR lines were acquired across three different locations along with one seismic line in the active quarry in Undheim. The interpretation of the GPR lines was made in the same way as it would be made in a seismogram, looking for the strongest reflectors in the radargram and associating them to different lithologies or materials. The seismic inversion was made with first arrival traveltime tomography and with full waveform inversion providing similar results in the location of the main structures.

The combined results showed a good inversion in both methods with consistent results. The most important result was the correct mapping of the basement in the area: GPR, first arrival traveltime tomography, and full waveform inversion concurred in the depth location. GPR provided the best results mapping the glacial stratigraphy given the good lateral resolution obtained in the final results. In the radargrams it was possible to observe depositional features which were not visible in the seismic.

As future work, a denser GPR grid should be acquired and a geomodel could be constructed to map the location of the glacial sediments in the subsurface. Seismic data could be used as quality control for the depth converted radar lines.

References

Annan, A. (2005). Ground-penetrating radar. In *Near-surface geophysics* (pp. 357–438). Society of Exploration Geophysicists.

Annan, P. (2003). Ground penetrating radar principles, procedures and applications. *Sensors and software*, *278*.

Benn, D. & Evans, D. (2010). Glaciers and glaciation. (pp. 680–685). Hodder Education.

Birkeland, T. (1981). The geology of Jæren and adjacent districts. A contribution to the Caledonian nappe tectonics of Rogaland, southwest Norway. *Norsk Geologisk Tidsskrift*, *61*(3-4), 213–235.

Booth, A. D., Mercer, A., Clark, R., Murray, T., Jansson, P., & Axtell, C. (2013). A comparison of seismic and radar methods to establish the thickness and density of glacier snow cover. *Annals of Glaciology*, *54*(64), 73–82.

Burstedde, C. & Ghattas, O. (2009). Algorithmic strategies for full waveform inversion: 1D experiments. *Geophysics*, *74*(6), WCC37–WCC46.

Chen, P. (2011). Full-wave seismic data assimilation: theoretical background and recent advances. *Pure and applied geophysics*, *168*(10), 1527–1552.

del Valle Toledo, E. (1984). Introduccion a los metodos geofisicos de exploracion. In UNAM (Ed.), (Chap. 6, pp. 143–188). Apuntes Facultad de Ingenieria. Division de Ingenieria en Ciencias de la Tierra.

Direktoratet for mineralforvaltning. (2014). Søknad om driftkonsesjon. Retrieved March 14, 2018, from http://docplayer.me/63593121-Saeland-massetak-i-time-kommune.html

Fisher, S. C., Stewart, R. R., & Jol, H. M. (1996). Ground penetrating radar (GPR) data enhancement using seismic techniques. *Journal of Environmental and Engineering Geophysics*, *1*(2), 89–96.

Fredin, O., Bergstrøm, B., Eilertsen, R., Hansen, L., Longva, O., Nesje, A., & Sveian, H. (2013). Glacial landforms and Quaternary landscape development in Norway. *Quaternary Geology of Norway. Geological Survey of Norway, Special Publication*, *13*, 5–25.

Google. (n.d.). [Google Earth satellite view of Jæren]. Retrieved May 7, 2018, from https://earth.google.com/web/@58.7388034,5.91315628,179.3788529a,122554.39948641d,35y,0h,0t,0r

Helleve, E. (2017). Time kommune, Rogaland. Retrieved May 28, 2018, from https://www.allkunne.no/framside/geografi/noreg/kommunar/time-kommune-rogaland/23/810/

Jiang, W. & Zhang, J. (2017). 3D first-arrival traveltime tomography with modified total-variation regularization. *Journal of Geophysics and Engineering*.

Jol, H. (2009). Ground Penetrating Radar. (Chap. 1, 4-7 and 33-37). Elsevier.

Kearey, P., Brooks, M., & Hill, I. (2013). An introduction to geophysical exploration. (Chap. 3, pp. 21–32). John Wiley & Sons.

Knudsen, C. G., Larsen, E., Sejrup, H. P., & Stalsberg, K. (2006). Hummocky moraine landscape on Jæren, SW Norway—implications for glacier dynamics during the last deglaciation. *Geomorphology*, *77*(1-2), 153–168.

Koson, S., Chenrai, P., & Choowong, M. (2014). Seismic attributes and their applications in seismic geomorphology. *Bulletin of Earth Sciences of Thailand*, *6*(1), 1–9.

Malå GeoScience. (2005). RadExplorer 1.4 User manual. Retrieved February 12, 2018, from https://www.guidelinegeo.com/wp-content/uploads/2016/07/RadExplorer14_user_manual_ENG.pdf

McQuillin, R. (1984). An introduction to seismic interpretation : reflection seismics in petroleum exploration. (2nd ed., Chap. 2, pp. 9–26). London: Graham & Trotman.

Nichols, G. (2009). Sedimentology and stratigraphy. (Chap. 7, pp. 102–110). John Wiley & Sons.

Norges Geologiske Undelsøkelse. (2018). [Kart min kommune]. Retrieved February 6, 2018, from http://geo.ngu.no/kart/minkommune/

Norwegian Meteorological Institute. (2018). [Tabular view for temperature and precipitation per month in Stavanger]. Retrieved June 8, 2018, from https://www.yr.no/place/Norway/Rogaland/Stavanger/Stavanger/statistics.html

Olsen, L., Sveian, H., Ottesen, D., & Rise, L. (2013). Quaternary glacial, interglacial and interstadial deposits of Norway and adjacent onshore and offshore areas. *Quaternary Geology of Norway, Geological Survey of Norway Special Publication*, *13*, 79–144.

Raunholm, S., Sejrup, H. P., & Larsen, E. (2003). Lateglacial landform associations at Jæren (SW Norway) and their glaci-dynamic implications. *Boreas*, *32*(3), 462–475.

Sheriff, R. E. (1995). Exploration seismology. (2nd ed., Chap. 2, pp. 33–38). Cambridge: Cambridge University Press.

Singh, K., Kulkarni, A., & Mishra, V. (2010). Estimation of glacier depth and moraine cover study using ground penetrating radar (GPR) in the Himalayan region. *Journal of the Indian Society of Remote Sensing*, *38*(1), 1–9.

The Norwegian Water Resources and Energy Directorate. (2018). Rainfall- monthly data. Retrieved May 28, 2018, from http://www.senorge.no/index.html?p=senorgeny&st=water

Tronicke, J. & Böniger, U. (2013). GPR attribute analysis: There is more than amplitudes. *First break*, *31*(8).

Zhu, J., Lines, L., & Gray, S. (1998). Smiles and frowns in migration/velocity analysis. *Geophysics*, *63*(4), 1200–1209.

Appendix

A1. Topography data

Sample data of topography accepted in software: *.txt files.

Trace number	Elevation (m)
2	249.3
3	249.3
4	249.3
6	249.3
9	249.2
12	249.2
13	249.3
15	249.2
17	249.2
20	249.2
23	249.2
26	249.2
29	249.2
31	249.2
33	249.2
35	249.1
37	249.1
38	249.1
40	249.1
41	249.0
43	249.0
45	249.0

Table 4: Sample of topography of line 30 - Sandnes site